International Journal of Multiphase Flow 36 (2010) 513–532

Contents lists available at ScienceDirect

International Journal of Multiphase Flow

journal homepage: www.elsevier.com/locate/ijmulflow

Simulation of liquid jet primary breakup: Dynamics of ligament and droplet formation

J. Shinjo [a,*], A. Umemura [b]

[a] Numerical Analysis Group, Aerospace Research and Development Directorate, Japan Aerospace Exploration Agency, 7-44-1 Jindaiji-higashimachi, Chofu, Tokyo 182-8522, Japan
[b] Department of Aerospace Engineering, Nagoya University, Furo-cho, Chikusa-ku, Nagoya 464-8603, Japan

ARTICLE INFO

Article history:
Received 1 July 2009
Received in revised form 15 January 2010
Accepted 27 March 2010
Available online 1 April 2010

Keywords:
DNS
Primary breakup
Ligament
Droplet

ABSTRACT

Primary atomization of liquid injected at high speed into still air is investigated to elucidate physical processes by direct numerical simulation. With sufficient grid resolution, ligament and droplet formation can be captured in a physically sound way. Ligament formation is triggered by the liquid jet tip roll-up, and later ligaments are also produced from the disturbed liquid core surface in the upstream. Ligament production direction is affected by gas vortices. Disturbances are fed from the liquid jet tip toward upstream through vortices and droplet re-collision. When the local gas Weber number is O(1), ligaments are created, thus the ligament or droplet scale becomes smaller as the bulk Weber number increases. Observation of droplet formation from a ligament provides insights into the relevance between the actual droplet formation and pinch-off from a slow liquid jet in laboratory experiments. In the spray, the dominant mode is the short-wave mode driven by propagative capillary wave from the ligament tip. An injection nozzle that is necessary for a slow jet is absent for a ligament, thus the long-wave (Rayleigh) mode is basically not seen without the effect of stretch. By the present simulation, a series of physical processes have been revealed. The present result will be extended to LES modeling in the future.

1. Introduction

Liquid atomization is an important process in engineering applications such as aerospace propulsion systems, automotive engines, food processing, and inkjet printing. For engine applications, the fuel spray characteristics are critical to determining the engine performance such as fuel consumption rate or exhaust gas cleanness. However, our understanding on physical mechanisms of liquid atomization is still not sufficient (Lin, 2003).

An actual turbulent spray includes multi-scale physical processes. In the liquid core region, the dense liquid column is affected by aerodynamic interaction. The liquid surface becomes unstable and ligaments are created. From these ligaments, droplets are created. This process is usually called primary breakup. After primary breakup, it is generally believed that large droplets may break into smaller droplets and this process is called secondary breakup. Droplets also become smaller by evaporation and finally combustion takes place. The spatial scale becomes smaller as the liquid flows downstream following the above-mentioned processes. The final droplet production is greatly dependent on primary breakup, but it has been difficult to know what is actually occurring in the primary breakup region.

Experimentally, observing this dense and small region with high spatio-temporal resolution has been difficult. Several papers have reported recent experimental efforts in observing the primary breakup region to understand its physics. For example, two-dimensional images of the near field of a Diesel spray were obtained by Linne et al. (2006), but primary droplets were smaller than the resolution limit. Image analysis technique was used in Blaisot and Yon (2005) to characterize the droplet size. Velocity measurements were conducted to understand the dense spray near the nozzle (Chaves et al., 2004). So far, the entire physics has not been unveiled yet by experiments and further efforts are continuing.

In numerical simulation, it has been also difficult to know the primary breakup phenomena because the resolution requirement is severe especially for high Weber and Reynolds numbers. Surface tension plays an important role in ligament and droplet formation. To resolve such processes, the local shape (i.e., curvature) of ligaments or droplets should be captured correctly. If the resolution is not sufficient, physically wrong results will be obtained. Due to the lack in primary atomization knowledge, existing numerical spray models for Reynolds-averaged Navier–Stokes simulations (RANS) or large-eddy simulations (LES) are made with drastic simplifications. For example, one of the present spray simulation models starts from assuming large (even the scale of injector diameter)

* Corresponding author. Tel.: +81 422 40 3316; fax: +81 422 40 3073.
E-mail addresses: shinjo.junji@jaxa.jp (J. Shinjo), akira@nuae.nagoya-u.ac.jp (A. Umemura).

0301-9322/$ - see front matter © 2010 Elsevier Ltd. All rights reserved.
doi:10.1016/j.ijmultiphaseflow.2010.03.008

blobs at the injector exit and their breakup. Such models have enabled practical-scale engineering simulations, but the assumptions are sometimes different from the actual primary breakup physics. Parameter tuning is usually necessary with reference experimental data, and this should be done every time when the flow conditions are changed. Such a simulation methodology is not closed by itself and includes many model parameters that are dependent on flow fields. If reference experimental data are unavailable, these parameters must be arbitrarily determined.

The following knowledge about turbulent spray is still lacking or insufficient. (1) Development of surface instability. What triggers instability and how it leads to atomization needs further investigation. In experiments, several disturbances may usually exist at the same time. In numerical simulation, an ideal flow setting is possible. This may enable us to understand the mechanism in a straightforward way. (2) Ligament formation mechanism. There have been reports that observed ligament formation in slow liquid jets (Sallam et al., 2002, Marmottant and Villermaux, 2004). Especially for high *We* and small-scale sprays, data are almost unavailable. (3) Droplet formation mechanism from a ligament. The present status is the same as that of (2). Furthermore, the relevance between laboratory experiments using slow liquid jets (such as in the Rayleigh instability analysis) and actual ligaments has not been discussed well. Better knowledge of primary breakup will lead to better predictions of spray characteristics such as initial droplet size distribution, spray angle and the jet structure, thus this is strongly needed.

To breakthrough such a situation, we have conducted several research efforts. Corresponding to the above (3), the dynamics of droplet formation from a single ligament has been investigated by using a slow round liquid jet issued from a nozzle (Umemura and Wakashima, 2002; Umemura, 2004a,b, 2007a,b,c, 2008; Shinjo et al., 2009) (also see Section 3.4). Umemura (2007a,b,c)) has pointed out the importance of the role of the propagative capillary waves in the region of $We \sim O(1)$. This is a point that has been overlooked by the conventional understanding. The injection nozzle also has a certain effect on droplet pinch-off dynamics. This will be later discussed.

The next step to be investigated toward a full spray simulation is to elucidate how surface instability grows (corresponding to (1)), how ligaments are created from the liquid jet surface (corresponding to (2)) and what is the relevance between the slow jet experiments and actual ligaments (corresponding to (3)). The objective of this study is to investigate the above three points of primary breakup in high-speed liquid jets. Direct numerical simulation (DNS) is conducted for this purpose. A simplified configuration of round liquid injection into still air is considered here**.** The injection velocity is set close to that of actual engine devices. This paper especially focuses on the physical dynamics of ligament and droplet formation occurring near the jet tip. Statistical analysis and modeling proposals will be presented in a next report. Information obtained in this simulation will be extended in the future to modeling for LES, which is the only choice today for practical engine simulations. There have been many efforts in LES modeling. See Pan and Suga (2006), for example. However, LES still needs improvement in formulation and modeling.

Even if the liquid jet core size is small, the requirement for grid resolution in DNS is severe as mentioned above. The local Weber number varies drastically from $We \gg 1$ in the nozzle exit region to $We \ll 1$ in the downstream region. As pointed out by Gorokhovski and Herrmann (2008), using adequate topology-change models, the smallest scale to be resolved is of the order of the smallest droplets and ligaments. If the grid resolution is not enough, artificial (or fake) breakup may occur, i.e., when the thickness of some local liquid structure becomes smaller than the grid spacing, apparent numerical breakup occurs that is totally unphysical. "Resolved" means that there should be enough grid points to know the local shape and curvature. Surface tension is the force that induces breakup and this should be evaluated correctly (see also Section 2.3).

Droplets of O(1 μm) are usually generated by liquid fuel injection through a 0.1–0.2 mm diameter nozzle at the velocity order of 10 or 100 m/s. Assuming that numerical mesh spacing should be around, say, one-fifth of the diameter, or even smaller to capture the shape precisely, a uniformly-spaced grid system may require more than several hundred million grid points by a rough estimation. The number may become larger depending on Reynolds and Weber numbers of the flow. If the injection speed is increased, i.e., the bulk Weber number is increased, local structures will get smaller. Thus, more grid points are needed to resolve the related phenomena. In fact, one easy way to see whether a numerical result is physically correct or not is to examine whether wave creation on ligaments can be seen and round (spherical) and oscillating droplets can be observed, which indicates the preciseness of local surface tension evaluation.

There have been several efforts to date in the context of primary breakup simulation. Menard and coworkers (Menard et al., 2007, Lebas et al., 2009) have reported the dynamics of a liquid jet injected into still gas using the coupled level set/VOF/ghost fluid methods. As pointed out by Gorokhovski and Herrmann (2008), the grid resolution was coarse for the chosen Reynolds and Weber numbers, so this was not a direct numerical simulation in a true sense. The produced ligaments and droplets did not exhibit smooth shapes or wave dynamics driven by surface tension. But the overall liquid jet motion was captured in this simulation. Desjardins also applied the combined level set/ghost fluid method (Desjardins et al., 2008) to a straight jet configuration and to a temporally evolving planar liquid jet (Desjardins, 2009). Pai et al. (2008) have also reported primary breakup simulation results of cross flows. The grid system had 100 million grid points for the maximum *We* number case, and the phenomenon was well resolved for the target flow conditions. Herrmann's studies are also one of the most advanced in this field. A balanced force technique for Level Set methods was proposed and demonstrated for accurate interface tracking (Herrmann, 2008a). Straight jets and subsonic liquid cross jets were investigated in detail (Herrmann, 2008b, 2009a,b,c) using very fine grid systems. The bulk jet characteristics were discussed in detail and the grid convergence study on droplet size distribution showed that the result became better for a finer grid resolution. Thus, Herrmann concluded that "numerically induced topology change starts to mimic the physical breakup mechanism on small scales" when the grid resolution was fine (Herrmann, 2009b). The Lagrangian treatment of produced droplets is also a promising way to allow for full two-way coupling and continued secondary atomization. The effect of air/liquid density ratio on jet penetration length and breakup characteristics was also investigated (Herrmann, 2009c). These results have demonstrated the effectiveness of DNS study in primary breakup. The present study extends these efforts and discusses the physical mechanisms including ligament and droplet formation that still need further discussions.

Adaptive mesh refinement (AMR) is another option to conduct three-dimensional primary breakup simulations. Although interpolation incidental to grid transformation may introduce numerical errors and there is an ambiguity in determining which region to put more (or fewer) grid points, required computer resource can be reduced. Thus, this technique can be a useful tool in conducting practical-scale simulations. Fuster et al. (2009) have reported several numerical results of primary breakup using an adaptive mesh refinement technique. Their results are in fairly good agreement with experimental data. Here, however, to reduce numerical complexities to the minimum, this approach is not used.

In the following sections, flow setup, numerical methods, numerical results and discussion will be presented.

2. Simulation setup

2.1. Target flow configuration

First, the name definitions in this paper are shown in Fig. 1. Fig. 1a is about the entire liquid jet. The liquid core refers to the main liquid column issued from the nozzle. The tip is the front part of the liquid core and the tip edge denotes the edge of the rolled-up mushroom shape. A ligament, generated from the liquid tip edge or core, has ends and they are called ligament tips as shown in Fig. 1b. There are two directions in which surface tension works on a ligament. Surface tension in the generating line direction works to recover the neck (i.e., the neck radius will increase) and surface tension in the circumferential direction works to develop the neck (i.e., the neck radius will decrease).

Liquid jet injection into quiescent high-pressure air is considered here. Considering an automotive fuel injector, the flow conditions are set as shown in Table 1 (Rantanen et al., 1999). However, the result can be extended to general liquid jets.

The injection nozzle is a round and flat (non-converging) nozzle with the diameter of 0.1 mm. Three injection velocities of 30 m/s, 50 m/s, and 100 m/s are tested, thus the liquid Weber number based on the nozzle radius ranges from 1270 to 14,100. The initial jet shape is set as a liquid cylinder of the length of the nozzle diameter.

The main objective here is to elucidate the physical mechanism in terms of cause-and-effect, so nozzle disturbances are not added in this study. The velocity profile of injected liquid is set flat. By this, instability should be naturally excited by air–liquid interaction. In actual situations, there are many disturbance sources, such as inner-nozzle turbulence, cavitation, and fuel supply oscillation. Ligament or droplet breakup occurs faster due to these factors (Badock et al., 1999, Stahl et al., 2006, Suh and Lee, 2008), but as a first step such factors are not included. This is not to say that nozzle disturbances are not important. In actual devices, nozzle disturbances are positively utilized. But, especially for Diesel injectors where fuel injection is intermittent, two factors exist for atomization. One is from the front tip of the jet and the other from the nozzle. The two effects are all mixed up in reality, and this situation makes the analysis more difficult because the cause-and-effect relation would become more complicated. In this study, the tip front effect is concentrated on. It is expected that the formation of mushroom-shape front tip would occur and this is the only result of the impact of the jet front onto the gas, not from the nozzle. It is also expected that even without disturbances from the upstream nozzle, the highly disturbed region behind the tip conveys the disturbances through the gas phase and causes atomization from the core. Which (front disturbances or nozzle disturbances) is dominant may depend on the strength of the imposed disturbances at the nozzle. Cases with nozzle disturbances will follow in the future to compare the effect.

The computational domain is a rectangular region. A Cartesian equidistant grid system is used for each case in this simulation. As the bulk Weber number increases, the number of required grid points increases because the local structures could become smaller. Table 2 shows the number of grid points, grid resolution and the domain size. The spatial spray evolution is slower for relatively smaller bulk *We*, thus the computational domain is set slightly different for each case. This level of fine grid resolution is applied for the first time in high bulk *We* primary breakup simulation. The present domain size allows us to capture ligament and droplet generation from the tip edge and liquid core. Full disintegration of the liquid jets issued from a nozzle could not be captured within this domain size, but it is sufficient to discuss the physical mechanisms of atomization.

The computation was carried out on JSS (JAXA Supercomputer System). The system has 13,568 cores and its peak performance is 136TFLOPS. The largest computation of case 3 used 5760 cores for 410 h. Case 1 used 1280 cores and case 2 1920 cores for similar run times.

2.2. Numerical methods

The governing equations to be solved are three-dimensional Navier–Stokes equations

$$\nabla \cdot \mathbf{u} = 0$$
$$\rho\left[\frac{\partial \mathbf{u}}{\partial t} + (\mathbf{u}\cdot\nabla)\mathbf{u}\right] = -\nabla p + \mu\Delta\mathbf{u} + \mathbf{F}_{SV} \quad (1)$$

Table 2
Numerical setup.

Case	Total number of grid points	Grid resolution (μm)	Domain size in D
1	400 million	1.5	$21.7 \times 8.0 \times 8.0$
2	1.16 billion	0.75	$23.4 \times 4.7 \times 4.7$
3	6 billion	0.35	$14.6 \times 4.5 \times 4.5$

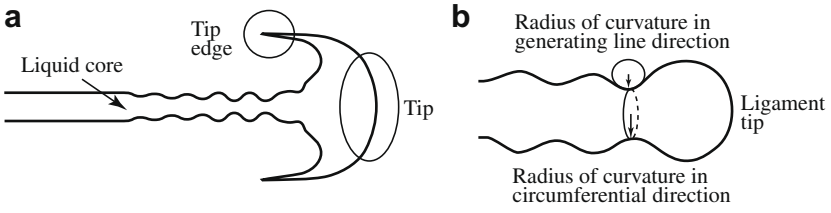

Fig. 1. Name definitions in this paper. (a) Liquid jet and (b) ligament.

Table 1
Flow conditions of liquid and gas.

Case	Nozzle diameter D (mm)	Ambient pressure p (MPa)	Gas density ρ_g (kg/m^3)	Liquid density ρ_l (kg/m^3)	Liquid viscosity μ_l (Pa s)	Gas viscosity μ_g (Pa s)	Surface tension coefficient σ (N/m)	Liquid velocity $U_l = U$ (m/s)	Gas velocity U_g (m/s)	Bulk liquid Reynolds number $Re_{bulk} = \rho_l U(D/2)/\mu$	Bulk liquid Weber number $We_{bulk} = \rho_l U^2(D/2)/\sigma$
1								30		440	1270
2	0.1	3	34.5	848	2870e−6	19.7e−6	30.0e−3	50	0	740	3530
3								100		1470	14,100

where $\mathbf{u}$ is the velocity vector, ρ the density, p the pressure and μ the viscosity. Pressure is obtained by solving the Poisson equation iteratively and the convergence criterion is set as the residual of 1.0e−10.

Both liquid and gas are treated as Newtonian fluids. $\mathbf{F}_{SV}$ is the surface tension term and evaluated by the Continuum Surface Force (CSF) method (Brackbill et al., 1992) as

$$\mathbf{F}_{SV} = \sigma\kappa\frac{\nabla\phi}{(\phi_{\max}-\phi_{\min})} \tag{2}$$

where σ is the surface tension coefficient, κ the local curvature and ϕ represents the color function with $\phi = 0$ for gas (g) and $\phi = 1$ for liquid (l). The density and viscosity are interpolated using ϕ.

$$\begin{aligned}\rho &= \phi\rho_l + (1-\phi)\rho_g \\ \mu &= \phi\mu_l + (1-\phi)\mu_g\end{aligned} \tag{3}$$

The color function ϕ follows the advection equation

$$\frac{\partial\phi}{\partial t} + (\mathbf{u}\cdot\nabla)\phi = 0 \tag{4}$$

The numerical scheme for solving flow advection is based on the Cubic Interpolated Pseudo-particle (CIP) method (Takewaki et al., 1985). The CIP method can capture a large density difference sharply and stably without numerical diffusion. The time step is restricted by flow velocity and surface tension (Brackbill et al., 1992; Sussman et al., 1994; Herrmann, 2008a), and it is chosen such that the CFL number based on the flow velocity is 0.3.

The phase interface is captured by the Level Set method (Sussman et al., 1994; Sussman and Puckett, 2000), i.e., the Level Set function (signed distance function) F is solved instead of directly solving ϕ. The liquid–gas interface is defined as $F = 0$, i.e., the distance is zero. F follows the advection equation.

$$\frac{\partial F}{\partial t} + (\mathbf{u}\cdot\nabla)F = 0 \tag{5}$$

F should satisfy

$$|\nabla F| = 1 \tag{6}$$

by its definition. But this is not always guaranteed due to numerical errors. To correct this, re-initialization (Sussman et al., 1994; Sussman and Puckett, 2000) process is implemented. Eq. (6) is satisfied by solving

$$\frac{\partial F}{\partial \tilde{t}} = sign(F)(1-|\nabla F|) \tag{7}$$

where $\tilde{t}$ is a virtual time and has no relation with the physical time t. Eq. (7) is transformed into

$$\frac{\partial F}{\partial \tilde{t}} + (\mathbf{U}\cdot\nabla)F = sign(F) \tag{8}$$

where $\mathbf{U} = sign(F)\mathbf{n}$ and $\mathbf{n}$ is the unit normal vector (Himeno and Watanabe, 2003). Eq. (8) is an advection equation, so the same numerical scheme CIP is used to solve Eq. (8).

A modified version of Volume-of-Fluid (VOF) method, called Multi-interface Advection and Reconstruction Solver (MARS) method (Kunugi, 1997), is combined with the above Level Set method to assure volume conservation (Sussman and Puckett, 2000; Himeno and Watanabe, 2003). The results of Level Set and MARS methods are used to complement each other. The same code has been used for slow liquid jet simulations in our previous work (Shinjo et al., 2007; Shinjo et al., 2009), whose results were in good agreement with experimental data (see Section 2.3).

2.3. Droplet pinch-off dynamics and grid resolution criterion

As already stated in Section 1, the primary objective is to see how ligaments and droplets are formed in the spray. The grid resolution of the present study is set so that this could be resolved (see Table 2). However, the term "resolved" should be treated with care, and this will be discussed later in this section.

Our previous study on droplet pinch-off from a ligament gives the criterion for the present grid resolution. A slow laminar liquid jet was studied in the microgravity environment to investigate the droplet pinch-off dynamics theoretically, experimentally and numerically (Umemura and Wakashima, 2002; Umemura, 2007a,b,c; Shinjo et al., 2009). The key role is played by propagative capillary waves. There are two modes of pinch-off, i.e., the short-wave mode and the long-wave (Rayleigh) mode. Which mode is dominant in a spray is an interesting topic in understanding atomization. The short-wave mode is a local mode in the vicinity of the jet tip (the short-wave mode was also termed end-pinching for Stokes flows in the literature (Stone et al., 1986, Stone and Leal, 1989a,b; Stone, 1994)). The pinch-off wavelength is close to that of the steady propagation wave given as (Umemura, 2007a)

$$\lambda = (2\pi/\sqrt{3})a_L = 3.62a_L \tag{9}$$

where a_L is the ligament radius. The steady wave can be naturally destabilized and pinch-off occurs. This mode basically does not require the role of injection nozzle. The long-wave (Rayleigh) mode is found to be driven by short and fast capillary waves from the jet tip. These waves must be reflected by the nozzle (if they can reach the nozzle overcoming viscous damping), and the wavelength becomes longer by Doppler shift due to the difference in relative velocities before and after reflection. Long-waves are unstable convectively, thus finally pinch-off occurs. This mode even occurs without any external disturbance input because the jet tip always generates propagative capillary waves. Of course, if forced from outside at the nozzle, this mode can also appear.

Fig. 2 shows the typical result (Shinjo et al., 2009). Fig. 2a and b shows the short-wave mode and long-wave mode, respectively, for a case with relatively high Ohnesorge number ($We = 1.4$, $Oh = 0.076$). The short-wave mode evolution is slow and pinch-off occurs sequentially from the tip. When the ligament length is large, the long-wave mode may appear. The representative stages in the short-wave mode are illustrated in Fig. 2c that corresponds to Fig. 2a case. The liquid jet tip contracts due to surface tension and pushes the inner part along the injection axis. In this stage, the tip bulb pressure is high. This motion emanates compression waves and the first neck (counted from the jet tip) grows (S-I). Along with this, the tip bulb grows because it absorbs the liquid from the upstream by contraction. As the tip bulb size grows, its inner pressure reduces and the tip bulb sucks the liquid further from the neck. This is rarefaction wave generation and the neck becomes thinner (S-II) accordingly. Finally, when the neck becomes thin enough, the circumferential surface tension cuts the neck (S-III). Fig. 2d shows more dynamic behavior of the short-wave mode in a case with relatively lower Ohnesorge number ($We = 1.7$, $Oh = 0.016$). The basic mechanism is the same as in the Fig. 2a case, but wave interaction with neighboring crests makes the phenomenon more complex (Shinjo et al., 2009). For both modes, capillary waves propagate toward upstream from the tip and droplet pinch-off is a final result of destabilization of these waves. Mode selection depends on the flow conditions such as the Weber and Ohnesorge numbers. Fig. 3 summarizes the above physical mechanism of both modes (Shinjo et al., 2009). The details are left to the references, but it can be said that the present simulation method could capture the pinch-off dynamics well. The same methodology is employed in this study.

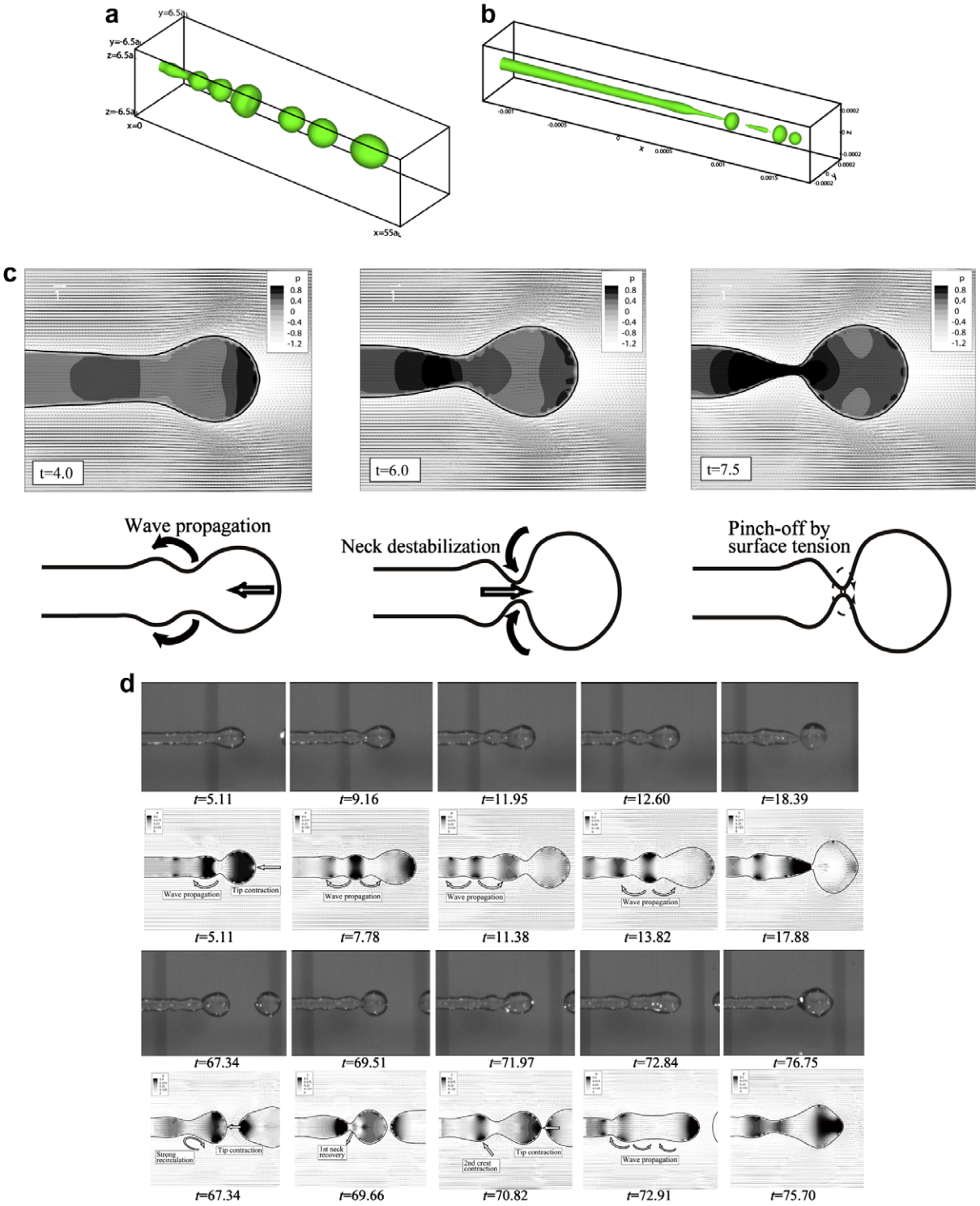

Fig. 2. Droplet formation from a slow liquid jet. The liquid flows from left to right. Two pinch-off modes are shown (Shinjo et al., 2009) in (a) the short-wave mode with the pinch-off wavelength $\sim 3.6a_L$ and (b) the long-wave (Rayleigh) mode with the pinch-off wavelength $\sim 9a_L$. Mode selection depends on the flow conditions. In (c), each stage of short-wave mode destabilization is shown with the computed pressure and velocity fields. In (d), the short-wave mode pinch-off with strong wave interaction for smaller *Oh* is shown (upper: "pattern A", lower: "pattern B").

These pinch-off phenomena are also expected to occur for ligaments in an actual highly-disturbed spray. For an actual ligament in the spray, the short-wave mode is expected to be dominant because a ligament has at least one end (tip) and no nozzle. Thus, wave patterns should appear on the ligament surface by tip contraction from the end(s). If the grid resolution is small enough to resolve the ligament or droplet diameter scale, the wave patterns should be correctly captured and generated droplets should become spherical (and oscillate), both due to surface tension. (This will be also discussed in 3.4.) In our previous study, it was found that the grid resolution of at least about eight points for ligament diameter was necessary to capture the above-mentioned droplet pinch-off dynamics.

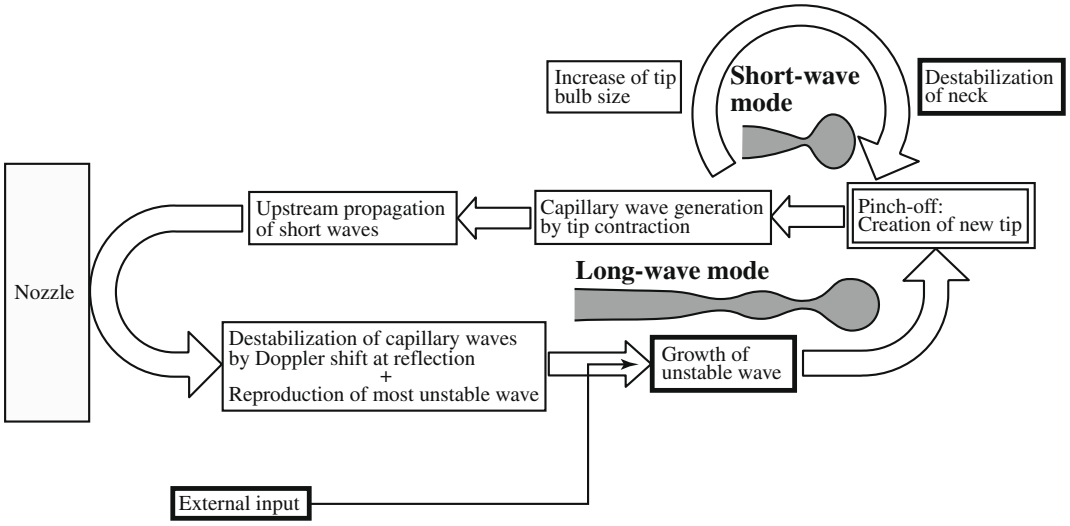

Fig. 3. Droplet pinch-off mechanism taken from reference (Shinjo et al., 2009). A slow liquid jet from an injection nozzle is assumed.

Herrmann clearly addresses the grid resolution issue in primary atomization simulation (Gorokhovski and Herrmann (2008), Herrmann, 2008a,b, 2009a,b,c). As pointed out there, no matter how small the grid spacing is, artificial droplets of the size of the grid spacing will be generated as long as this kind of Euler–Euler numerical formulation is used. When two interface fronts get closer than the grid spacing, breakup is automatically recognized regardless of the physics. The "exact" moment of breakup cannot be predicted and the generation of such artificial droplets depends on the local grid size. This error decreases with increasing grid resolution, but never becomes zero. The point is that these artificial droplets should be small enough and should not affect the focused dynamics dominantly, i.e., it should be the physics of surface tension that determines the most of ligament and droplet breakup.

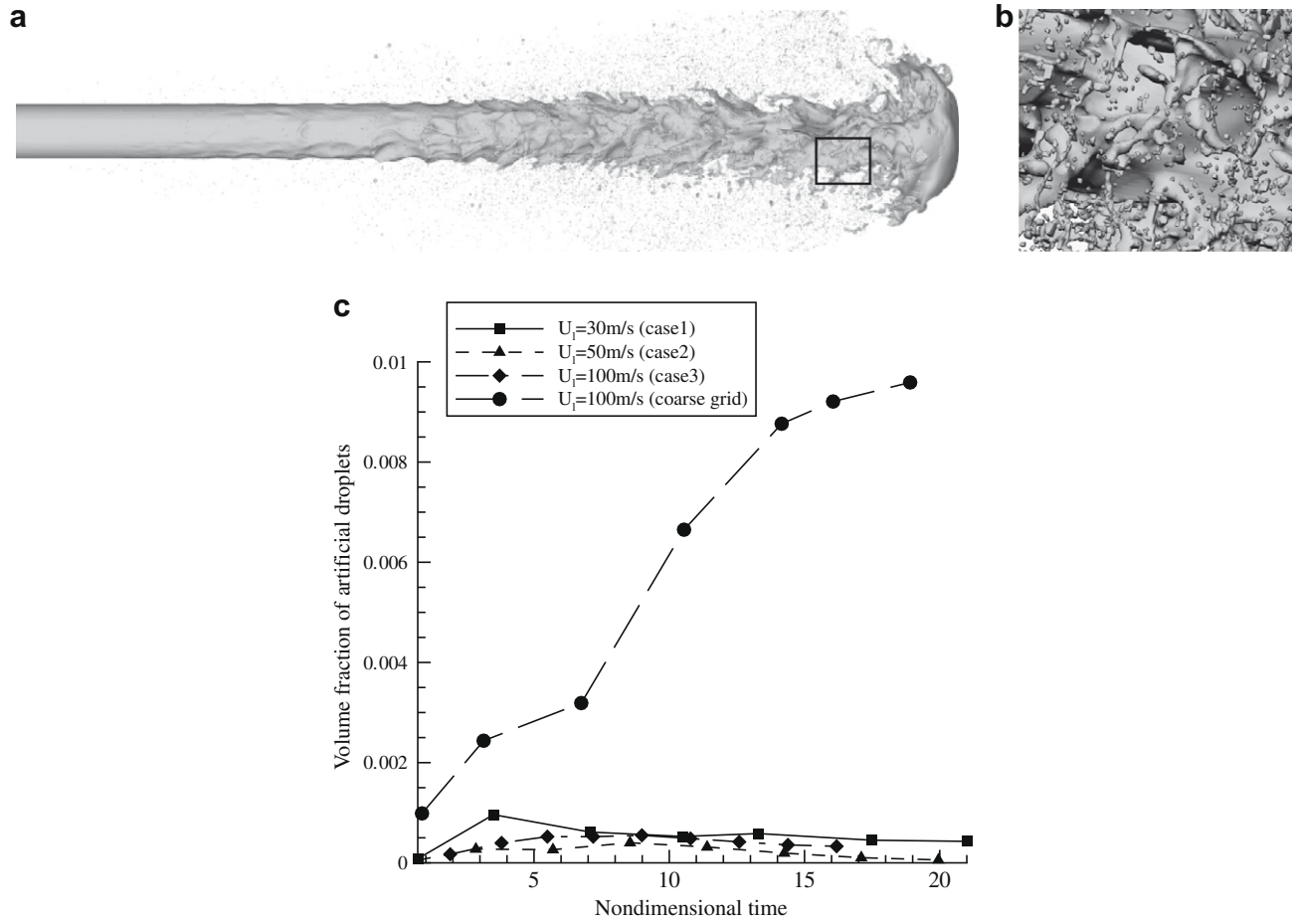

Fig. 4. Case 3 result with a coarse grid system (1.5 μm spacing). (a) Overall shape, (b) Zoom-up view, and (c) Temporal profiles of volume fraction of artificial droplets. The grid resolution is not sufficient because too many fragmented structures and artificial droplets are observed in (b). (c) shows the temporal profiles of volume fraction of artificial droplets to the existent total liquid volume for cases 1–3 and the above test case.

The grid resolution criterion for the present simulation is set so that the same level of resolution for each ligament and droplet is assured as in our previous study. The ligament and droplet dynamics is determined by the local Weber number, and $We \sim O(1)$ is expected. This condition cannot be completely known a priori, because the local velocity field is unknown beforehand. In this study, several cases are tested to determine the grid resolution. By the following considerations, it can be said that the present results capture the pinch-off dynamics well. But at the same time, we admit that a complete grid convergence study for all the cases considered is difficult because the present simulation requires a huge amount of supercomputer resources. The impact of numerical errors can be supposed to be small, but complete quantification may need future work.

First, for a grid resolution test, a test case with the grid spacing of 1.5 μm was conducted for the same flow conditions of case 3. Note that even this grid spacing is smaller than that used in Lebas et al. (2009) for almost the same flow conditions (the bulk *We* number in Lebas et al. (2009) was 11,600, thus it was a little smaller than the present case). Fig. 4 shows the result briefly. The overall spray seems reasonable at a first glance in Fig. 4a. But the close-up result in Fig. 4b implies that the resolution is not sufficient for small liquid structures like ligaments or droplets. Artificial or numerical breakup occurred, i.e., liquid structures broke into parts when the thickness of local liquid structure became smaller than the grid spacing. Many artificial droplets of the size of the grid spacing can be seen and unsmooth fragmented ligament shape shows that surface tension is not captured well. Thus, finer grid spacing should be used. In contrast to the above result, the result shown in Fig. 6 with six billion grid points shows smooth capillary wave patterns on the ligaments and round droplets, indicating sufficient grid resolution for capturing droplet pinch-off dynamics. In fact, 10 and more grid points are given for ligaments and droplets, and the observed dynamics is physically straightforward (see Section 3 for detail). There still remains room for discussion for the following estimation, but tentatively, an unresolved droplet is defined as a liquid structure that is smaller than four times the grid spacing ($4\Delta x$). Fig. 4c shows the temporal profiles of volume fraction of artificial droplets to the existent total liquid volume ($V_{artificial}(t)/V_{total}(t)$) for cases 1–3 and the above coarse case. The time is non-dimensionalized by the nozzle diameter D and liquid injection velocity U_l

$$t = t_{real}/(D/U_l) \tag{10}$$

The volume fraction increases up to 1% of the total volume in the above coarse case. (Note that this value would get even larger if artificial ligaments are included.) In the fine grid system (case 3), the fraction of artificial droplets remains less than 0.1% of the entire volume. The same level can be achieved in cases 1 and 2. Thus, as Herrmann (2009a) pointed out, with the increase of grid resolution and decrease of artificial droplets, the results of cases 1–3 reflect the actual physics. This will be strengthened by another test case shown next.

Second, the impact of artificial droplets is tested for case 1 where the fraction of artificial droplets is as small as that of case 3 discussed in the previous paragraph. (A test case of the same size was difficult for case 3 due to computer resource restrictions.) Here, a hypothetical case is considered where artificial droplets are erased upon production, i.e., an artificial liquid structure is replaced by the gas of the same velocity. The entire liquid volume cannot be conserved, thus in that sense, this is unphysical. However, the effect of artificial droplets can be known. Fig. 5 shows the instantaneous liquid shapes for both cases. It is clear that small artificial droplets are erased in Fig. 5b. But still, ligament formation and droplet formation from both the tip edge and the liquid core can be observed. Thus, the breakup is not driven or deterred by such artificial droplets. One minor difference lies in the instability development speed. The artificial droplets are small, but they surely have some mass and momentum and introduce disturbances. The development is slightly retarded when such droplets are erased from the flow field. This difference is not critical but leaves some room for future discussions, and it sets a future perspective.

From the above considerations, it can be said that the present simulation results represent most of the physics of primary atomization when keeping the fraction of artificial droplets at this low level. Based on this, the physical aspects are discussed in the following section.

3. Results and discussion

3.1. Overall structures

Fig. 6 shows the liquid surface shape near the liquid column tip region and the axial velocity magnitude in m/s for the three cases. In this region, the mushroom-shape tip is created due to the lateral liquid spread by impingement against the stagnant gas and roll-up

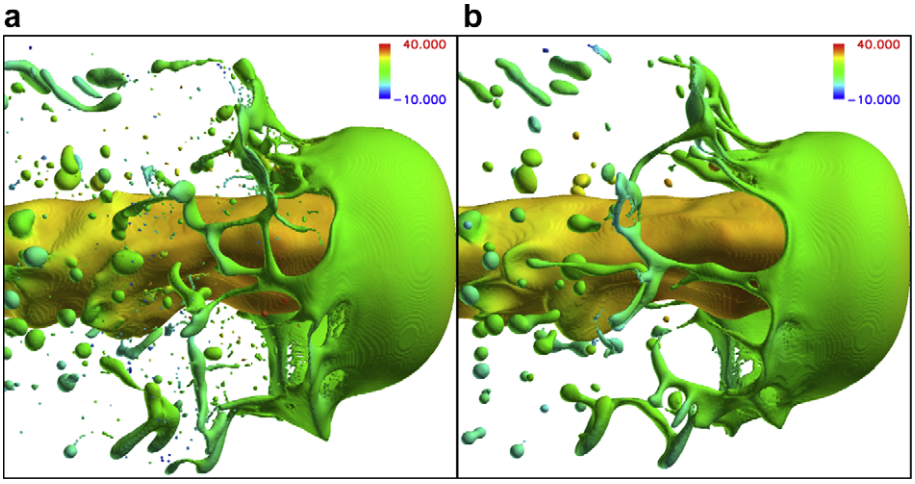

Fig. 5. Comparison of case 1 (left) with a hypothetical case where artificial droplets that are smaller than $4\Delta x$ are eliminated upon production (right). The color indicates the axial velocity in m/s. For both cases, $t = 16.59$.

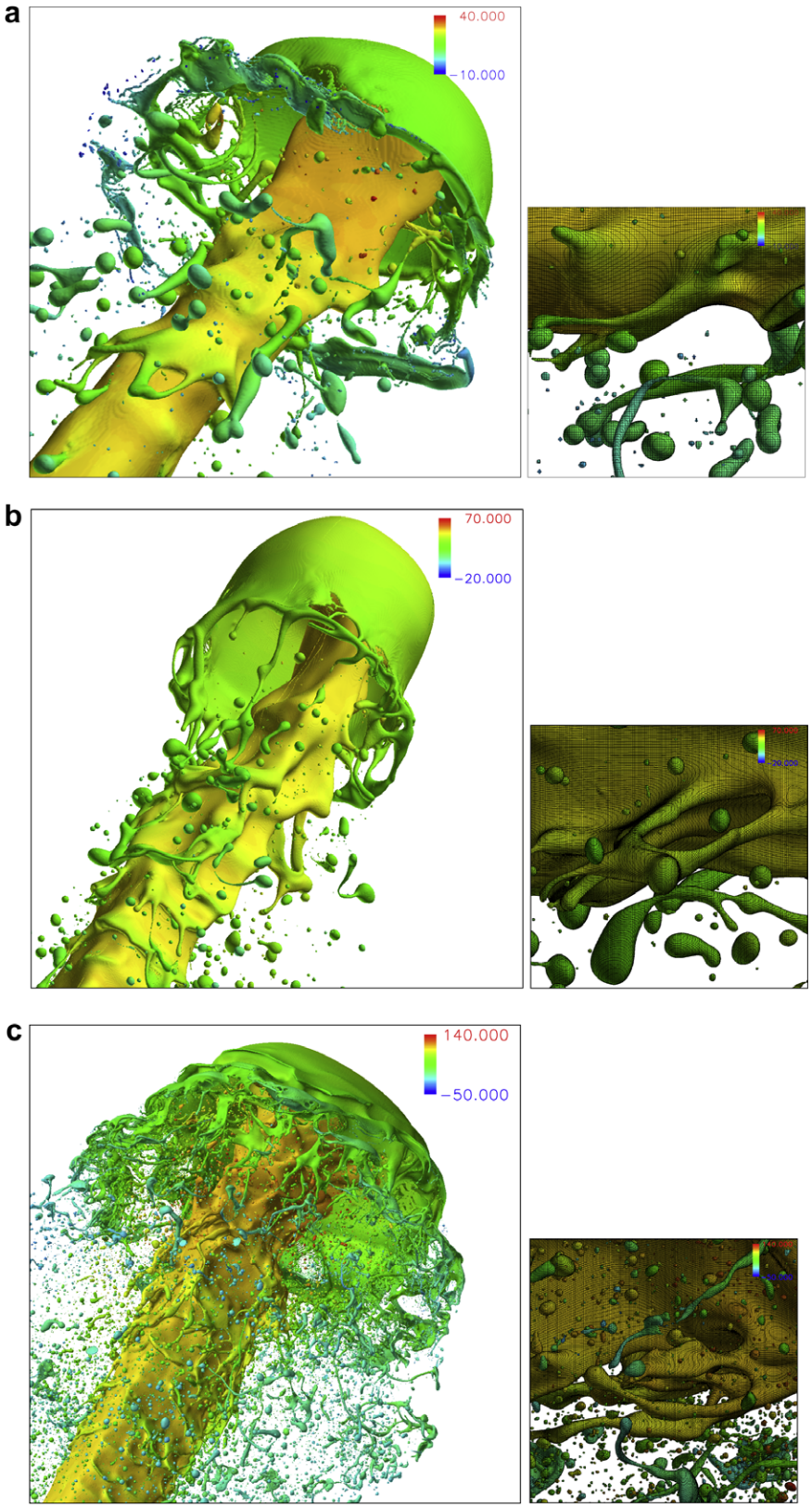

Fig. 6. The overall flow structure for each case. The color indicates the axial velocity in m/s. The grid resolution is indicated on the surface. (a) Case 1. The viewing range of the right figure is $1.8D \times 1.8D$. (b) Case 2. The viewing range of the right figure is $1.3D \times 1.3D$. (c) Case 3. The viewing range of the right figure is $0.7D \times 0.7D$.

by the initial Rayleigh–Taylor instability. Ligaments are first created from the edge of this rolled-up tip. Then, ligaments are also created from the liquid core surface. Droplet formation is observed from ligament tips. Thus, the main droplet size is strongly correlated to the ligament radius. Satellite droplets are created at the same time. These droplets are smaller than the main ones. Re-col-

lision of ligaments and droplets is often observed. This induces future ligament and droplet generation and makes the phenomenon more complicated.

The overall size of the generated liquid structures (ligaments and droplets) becomes smaller as the bulk Weber number increases. This will be later discussed in terms of the local Weber number. Spherical shape of droplets and smooth surface shape of ligaments shown in Fig. 6 indicate that the grid resolution is sufficient for each case.

Fig. 7 shows the temporal profiles of total liquid volume, total liquid energy and total liquid surface area for cases 1–3 and the coarse grid case of Fig. 4. The liquid volume is normalized by the injected volume. The overall trend is the same for all the cases. The volume error is less than or close to 1% and this value seems sufficiently small. For case 3, after $t > 10$ the decrease in the profile includes droplets going out of the computational domain. For the liquid energy, most of the energy is supplied as the kinetic energy and the surface energy is much lower because the bulk *We* is high. As the time passes, the kinetic energy reduces compared to the injected energy because part of the liquid kinetic energy is transformed into the gas kinetic energy, liquid surface energy and dissipation work. In the jet root region like in the present simulation, the liquid inertia is still strong, but as the jet goes further downstream, the liquid kinetic energy is expected to reduce further. The profiles of total liquid surface area show the increasing trend due to surface instability growth and atomization. The surface area of artificial droplets is not included. For the higher bulk *We*, the surface area increases faster. The coarse grid case also

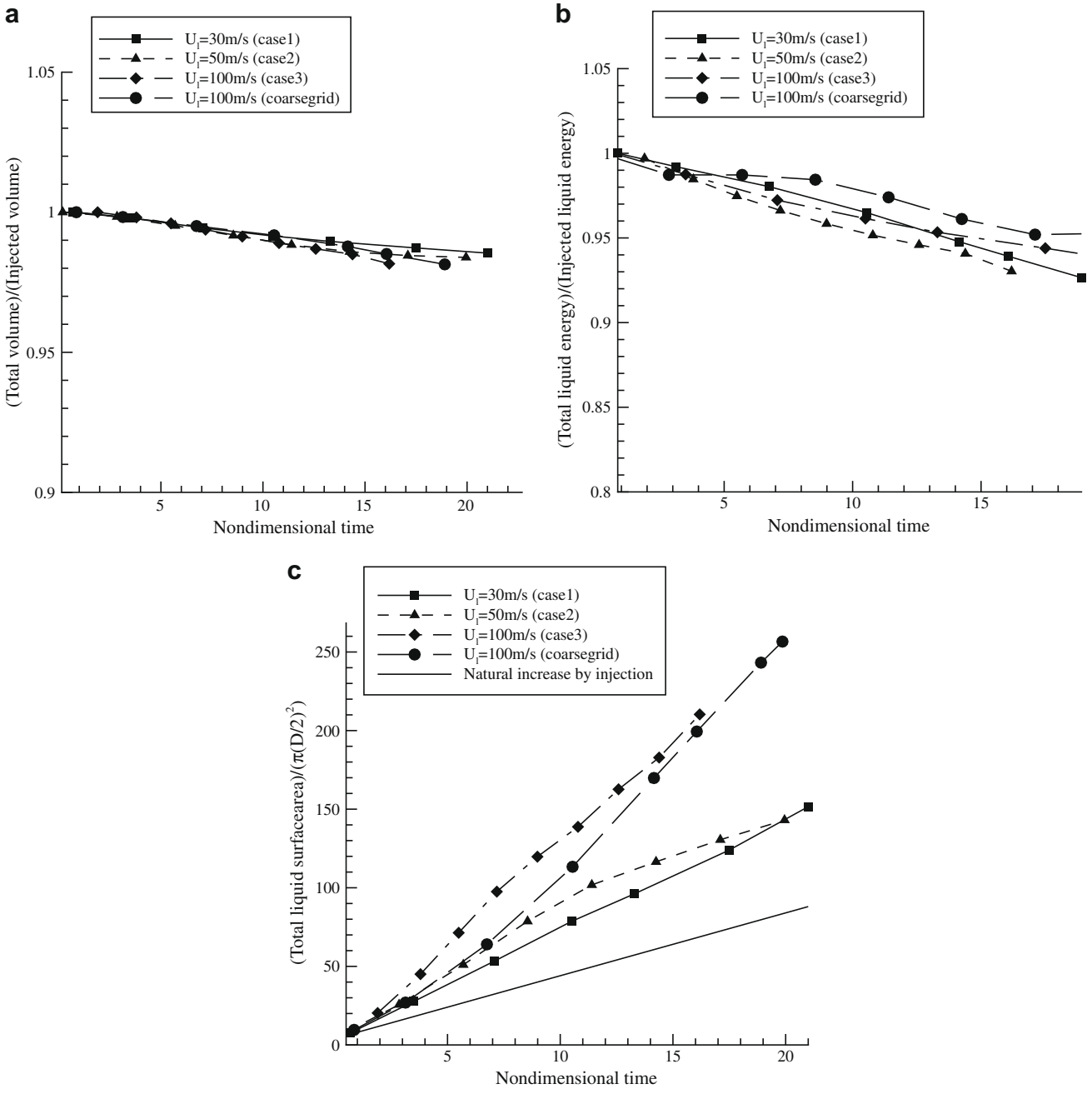

Fig. 7. Temporal profiles of (a) total liquid volume, (b) total liquid energy, and (c) total liquid surface area for cases 1–3 and the coarse grid case (with the same flow conditions as case 3 shown in Fig. 5).

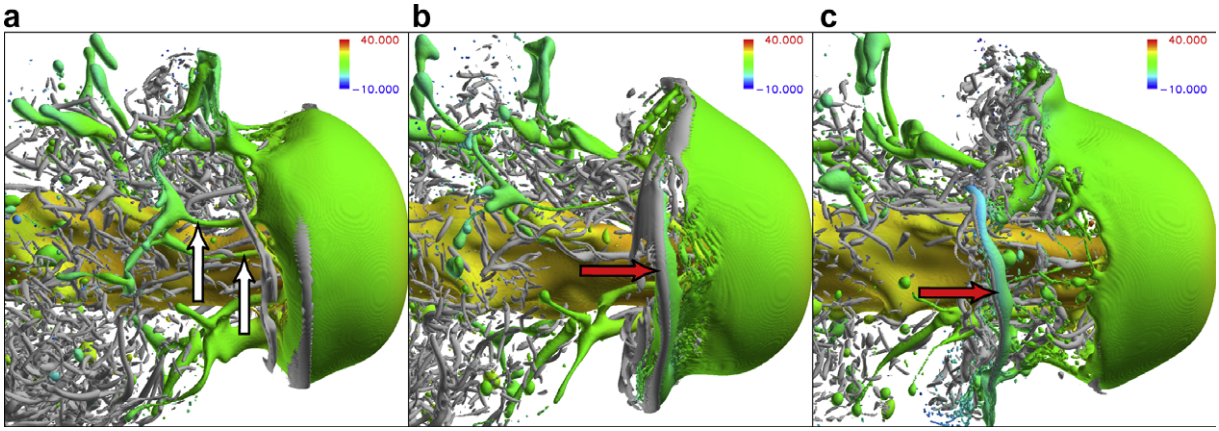

Fig. 8. Ligament formation from tip edge (case 1). Ligaments in the axial direction are indicated by the white arrow and a ring-like ligament by the red arrow. The flow is from left to right. Vortices (gray structures) are drawn by the second invariant of the velocity gradient tensor. (a) $t = 18.27$, (b) $t = 19.67$, and (c) $t = 21.07$.

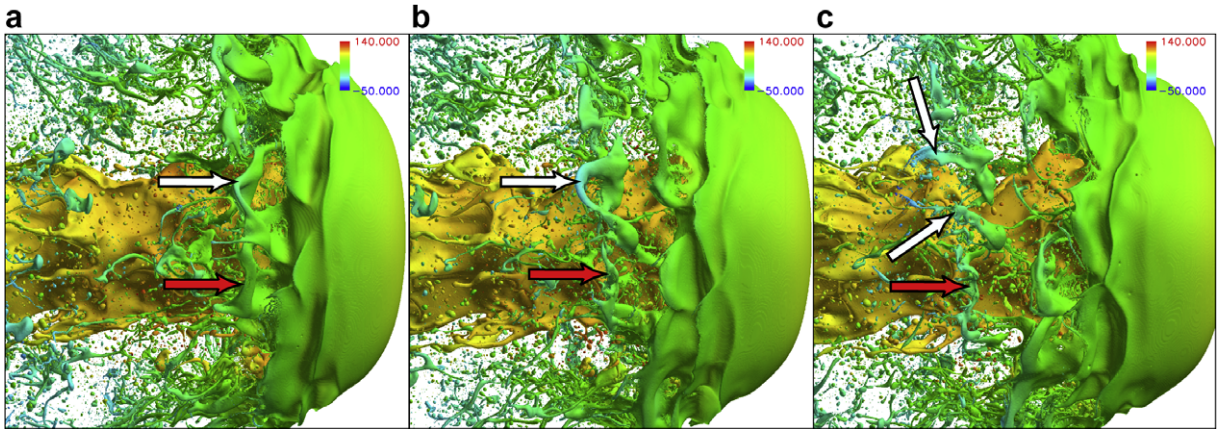

Fig. 9. Ligament formation from tip edge (case 3). Ligaments in the axial direction are indicated by the white arrow and a ring-like ligament by the red arrow. The flow is from left to right. (a) $t = 14.75$, (b) $t = 15.47$, and (c) $t = 16.19$.

shows a similar trend in surface area. This is caused by surface instability growth and ligament formation (although most ligaments are under-resolved). In this flow setup, the liquid jet gets longer as the time passes. The main atomization occurs at the tip edge of the front. Since the mass flow rate into the tip mushroom portion is small compared to the injection rate, the surface area increase seems small if the upstream liquid core is included like this. But when limited to the tip region only, the surface area increase is much larger due to atomization (Shinjo and Umemura, 2010). These trends are plausible and the present results represent the actual physics.

In the following sections, ligament formation, instability development and droplet formation are analyzed using mostly the results of cases 1 and 3.

3.2. Ligament formation

3.2.1. Ligament formation from tip edge

Ligament creation is strongly correlated with its local velocity field, as the strong shear near the liquid surface deforms the liquid surface. Thus, ligament formation first occurs from the tip edge.

At the first stage of injection, the liquid column tip rolls up in a mushroom shape. Strong axisymmetric vortices are formed behind this mushroom shape. Soon, streamwise vortices also emerge. These vortices interact and the flow field behind the tip mushroom becomes highly disturbed. Ligament formation is induced by local shear. The tip edge liquid sheet becomes thin as it is sheared and surface tension breaks up the sheet locally when $We \sim O(1)$. Nearby vortices determine the ligament formation direction. Axisymmetric vortices make ligaments normal to the injection axis and streamwise vortices make ligaments parallel to the injection axis. Fig. 8 shows this process in case 1. Streamwise ligaments are mainly seen in the first half indicated by the white arrows. There are many streamwise vortices in the vicinity. A fragmented ring-like ligament is created in the second half as shown by the red[1] arrow. This ligament is detached from the tip edge by vortices in the same direction. This kind of bag-like breakup at the tip edge has been also experimentally observed by, for example, Sallam et al. (2002).

Fig. 9 shows the time sequence of ligament formation from the tip edge in case 3. The flow field is much more disturbed, and more complex breakup can be observed. But the basic mechanism is the same. Generation of a fragmented ring-like ligament is shown by the white arrow in Fig. 9a and b. As the transverse instability wavelength is short, the ligament length is short. In Fig. 9c, this ligament breaks up into two pieces and turns into axial direction. For another ligament formation indicated by the red arrow, the process is almost the same, but it does not breakup into smaller pieces. The ligament generation process is strongly affected by the gas flow disturbances, so its nature is stochastic.

[1] For interpretation of color in Figs. 2, 5, 6, 8–12, 15, 18, 21–25, the reader is referred to the web version of this article.

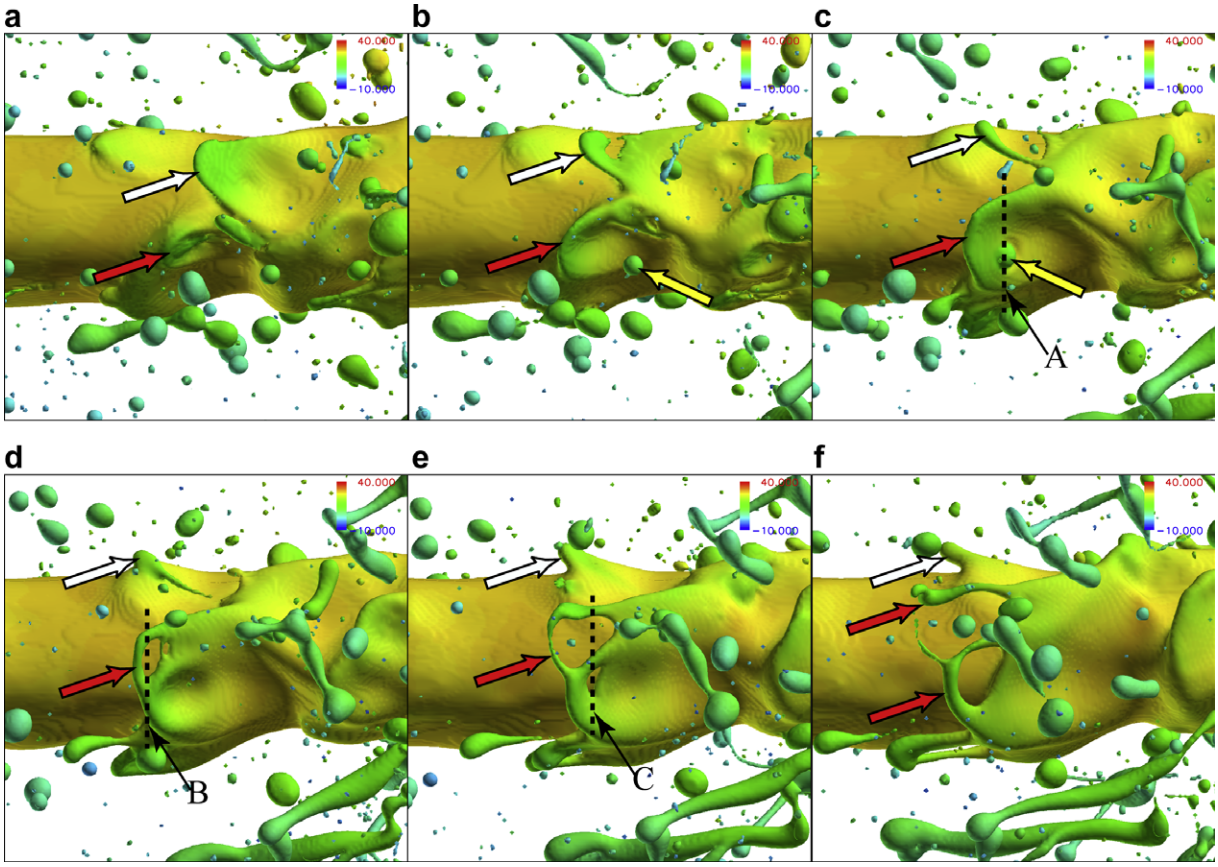

Fig. 10. Ligament formation from liquid core (case 1). The dashed lines (A–C) indicate the viewing regions of Fig. 11. The flow is from left to right. (a) $t = 17.57$, (b) $t = 18.27$, and (c) $t = 18.97$, (d) $t = 19.67$, (e) $t = 20.37$, and (f) $t = 21.07$.

The ligament formation is totally a three-dimensional phenomenon. As pointed out by Gorokhovski and Herrmann (2008), two-dimensional or axisymmetric simulations may overlook essential dynamics.

3.2.2. Ligament formation from liquid core

The crest formation on the liquid surface is due to the surface instability as will be discussed in Section 3.3. As the deformation grows on the liquid core, ligaments are also created from here. Fig. 10 shows ligament formation from the liquid core in case 1. Because the outer flow velocity is lower than the liquid core axial velocity, the crests are sheared by the aerodynamic force. Finally the most sheared part breaks up and ligaments are formed. Basically, such instability development and ligament generation is completed even only by the aerodynamic interaction. But in addition to that, generated droplets and ligaments sometimes re-collide with the liquid core surface again and feed disturbances to the surface. This motion is one factor to speed up the instability development. (Furthermore, if liquid turbulence is supplied at the nozzle, instability development is further enhanced.)

The white arrow indicates one example of crest development and ligament breakup. In this case, the crest breaks up into only one ligament. The crest is not smoothly transformed into a ligament but breaks up. The generated ligament soon detaches from

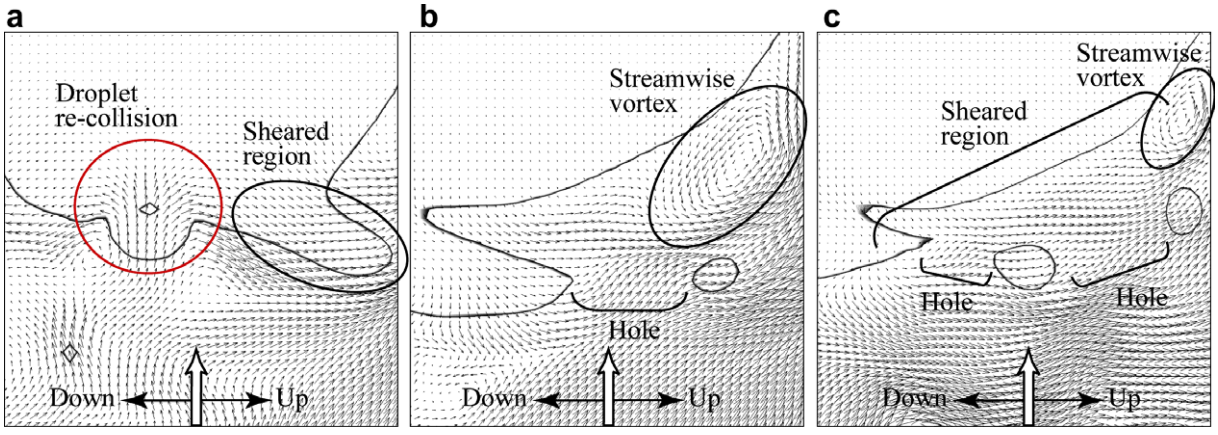

Fig. 11. Ligament formation (zoom). (a) Cross section A, (b) cross section B, and (c) cross section C. The arrows at the bottom indicate the viewing direction of Fig. 10.

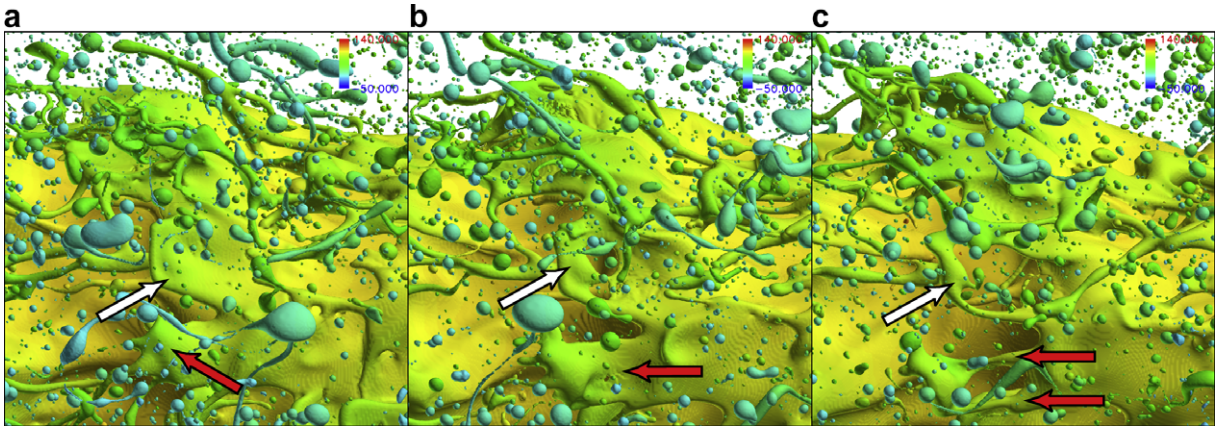

Fig. 12. Ligament formation from the liquid core (case 3). The color indicates the axial velocity in m/s. The flow is from left to right. (a) t = 15.76, (b) t = 16.33, and (c) t = 16.91.

the liquid core surface. It re-collides with the surface where a small crest has been already made (Fig. 10d). By this impact, another ligament development is enhanced. When only seeing Fig. 10e and f, it seems that one crest is transformed into one ligament (the white arrow), but this is not due to gas vortex motion, but due to the inertial motion from the re-collision.

The red arrow shows another example. In Fig. 10a, it can be found from the crest shape that ligament (or droplet) re-collision has initiated the crest development. Another impact occurs in Fig. 10c, as indicated by the yellow arrow. The crest develops rapidly after the impact. The central part of the flat crest soon becomes thinner than the rim because the rim is round and thicker due to surface tension. A hole is then created in the central region of the flat crest due to flow shear. Once a hole is made, it grows faster due to contracting motion by surface tension. By this, doughnuts-like shape is soon made. In this case, three ligaments are finally produced. The number of created ligaments depends on the initial crest shape, crest size and the local flow field.

Fig. 11 shows the three cross sections indicated by the dashed lines in Fig. 10c–e. As shown in Fig. 11a, the upper half of the crest has been already sheared. This makes a hole and finally a ligament indicated by the red arrow in Fig. 10d is generated. In Fig. 11b, the hole is also seen and a streamwise vortex to create the first ligament can be seen.

At the cross section A (Fig. 11a), the droplet re-collision is captured. The droplet impact induces vortices behind the droplet and sheared flows going apart from the impact point. The crest center becomes thinner by this motion. This creates another hole on the crest (Fig. 11c). The hole becomes larger as the time passes, leading to additional ligament formation.

Basically the same process can be observed in case 3, while the size of the generated ligaments is much smaller. Fig. 12 shows the result of case 3 by the white and red arrows. Crest development, shear effect by the gas, hole creation and final ligament generation can be observed similarly as in Fig. 10.

The typical ligament formation pattern from the liquid core surface is illustrated in Fig. 13. Multiple ligament formation from one crest is the most observed pattern in the simulation result. The local vortex motion shears the liquid surface and due to surface tension the round rim is likely to become thicker than the crest center. Further development makes a hole on the crest, finally leading to ligament formation.

3.2.3. Ligament scale and local flow field

The local gas Weber number of a ligament is defined here by

$$We_g = \rho_g |\mathbf{u}_l - \mathbf{u}_g|^2 a_L / \sigma \tag{11}$$

where $|\mathbf{u}_l - \mathbf{u}_g|$ is the magnitude of relative velocity between the liquid phase and gas phase. Locations (5–10) along the ligament axis are averaged. a_L is the baseline radius of the ligament, which is defined as the averaged radius throughout the ligament. We_g is a ratio of aerodynamic force to surface tension, thus it is expected that ligaments or droplets would be created when the two forces are comparable, i.e., $We_g \sim O(1)$.

The scatter plot of ligament baseline radius and local We_g is shown in Fig. 14 for the three cases. The points are somewhat scat-

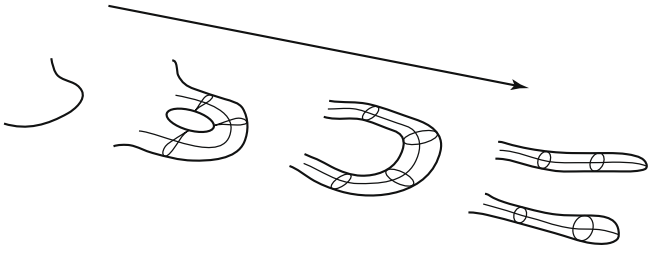

Fig. 13. Schematic illustration of ligament formation from the liquid core surface.

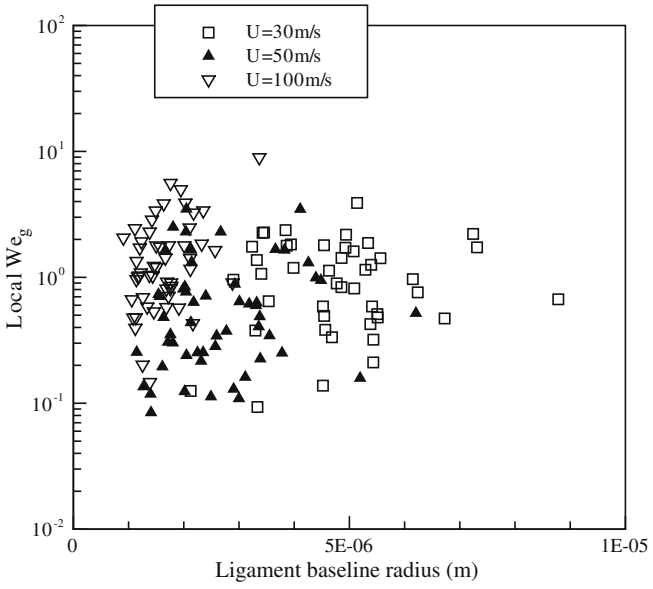

Fig. 14. Ligament baseline radius and local We_g for three cases.

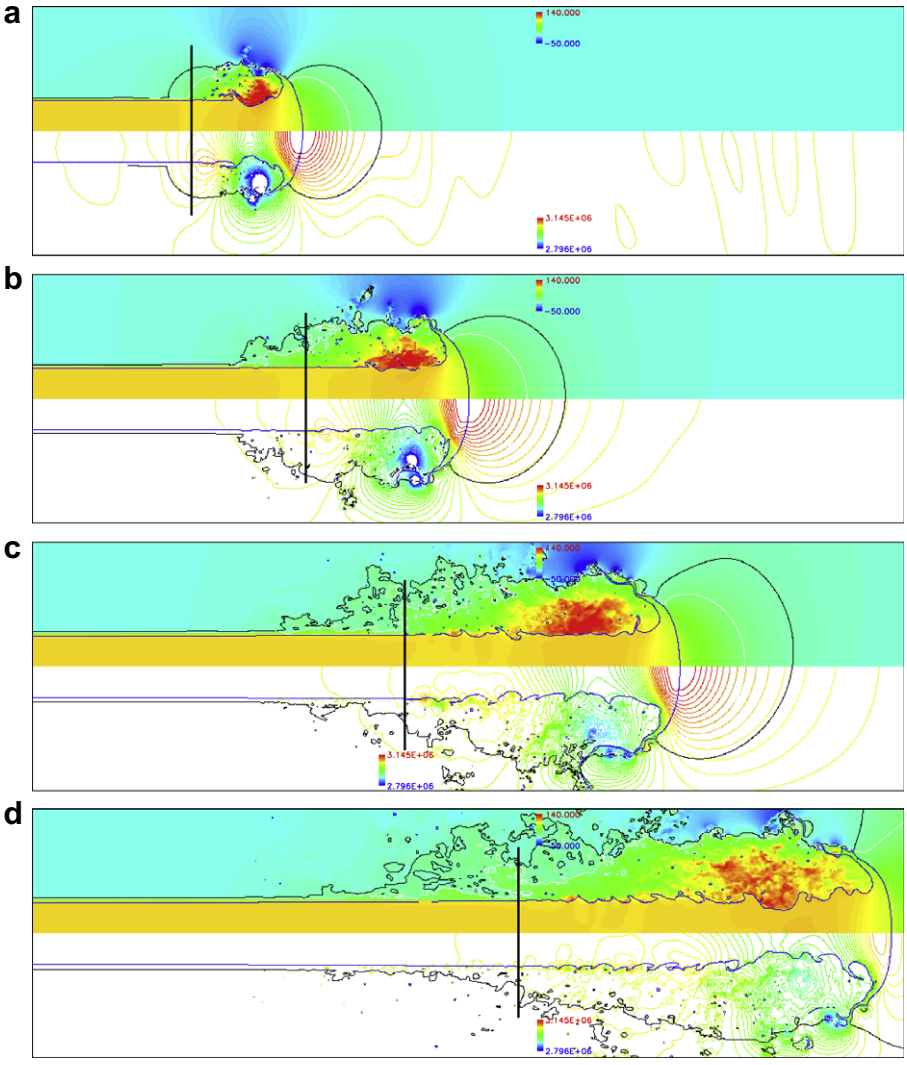

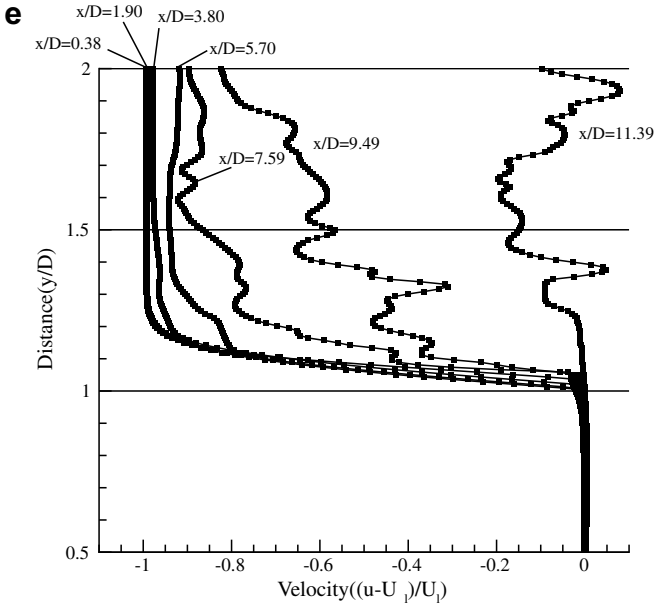

Fig. 15. (a–d) Axial velocity (upper half) and pressure (lower half) for case 3. The innermost blue line shows the liquid shape. The white line is an iso-line of 20 m/s ($0.2U_l$) and the outer black line 10 m/s ($0.1U_l$). (a) $t = 3.91$, (b) $t = 7.19$, (c) $t = 11.33$ and (d) $t = 15.47$. (e) Axial velocity profiles at $t = 15.47$.

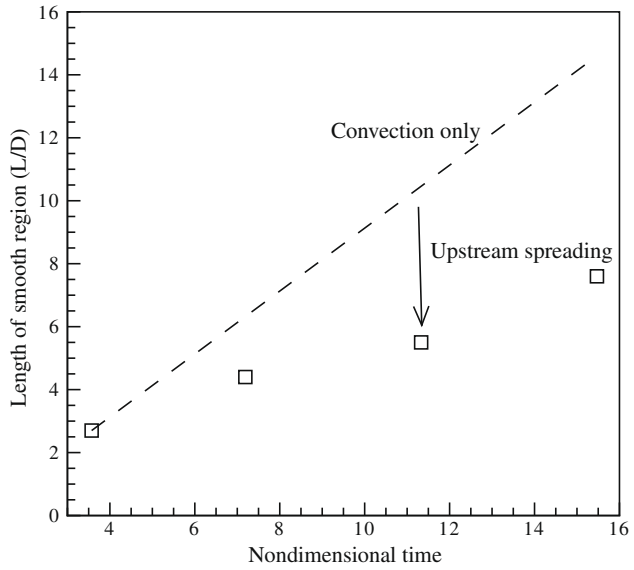

Fig. 16. Temporal plot of smooth region length for case 3. The dots are from the simulation result. The dashed line indicates simple convection at the injection velocity.

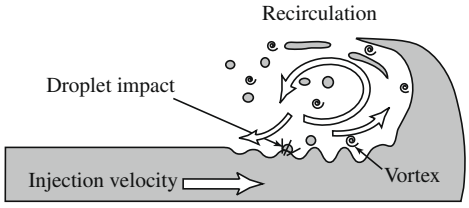

Fig. 17. Schematic of disturbance transmission paths.

tered in a certain range, but averagely they are around $We_g \sim O(1)$. When the liquid is broken into small pieces and the local We_g becomes O(1), surface tension makes the liquid elements into ligaments. The fragmented liquid elements become rapidly round thread-like shape due to surface tension.

As the bulk Weber number becomes larger, the ligament baseline radius becomes smaller. In fact, liquid elements are seeking the condition of $We_g \sim O(1)$, and if reached, they breakup into ligaments. Thus, the ligament baseline radius becomes smaller as the bulk Weber number becomes larger. The droplet size is strongly correlated to the ligament radius, as will be discussed in Section 3.4.

3.3. Development of surface instability

As the injection starts, the tip roll-up starts. In the very first moment, the roll-up is axisymmetric and a strong axisymmetric vortex is generated behind the tip. This is similar to a round jet of gas. The axisymmetry is soon broken by streamwise vortex development. Here, the development of surface instability is investigated, which is deeply related to the formation of ligaments and droplets.

Usually, when considering the development of surface instability, the growth of given disturbances is discussed. In the fuel jet configuration, disturbances are added at the nozzle and the convective development is considered. But naturally, the tip of the liquid column is the first region to be disturbed by the flow field, not the root of the liquid column. In terms of the cause-and-effect, the effect of disturbances from the tip region should be investigated first. In this study, the nozzle disturbances are eliminated for this purpose. In fact, this is only possible by numerical simulation.

Fig. 15 shows the temporal development of the liquid jet shape, the velocity field and the pressure field for case 3. At $t = 3.91$, a strong pressure rise in the tip region is generated due to the initial impact of the liquid column with the gas. The rolled-up tip creates a strong axisymmetric vortex behind it. This is also evident by the circular low pressure region behind the tip. (In the streamwise direction, many small vortices also exist.) Ligament formation from tip edge and also from the liquid core surface is already observed at this moment because these regions are exposed to strong shear from the gas. The liquid length is very short, thus this breakup is induced only by disturbances from the tip. As the time passes, this axisymmetric vortex gradually collapses, and the velocity field behind the tip becomes highly disturbed. But the global motion of recirculation behind the tip still remains. Namely, the axial gas velocity in the region just behind the tip is faster than the injection velocity and the gas velocity in the outer and upstream region is slower than the injection velocity.

At $t = 3.91$, the disturbed region is only limited to the tip region. The black line in Fig. 15 indicates the boundary between the undisturbed (smooth) surface and disturbed surface. This boundary is set at the position where the first ring-like wave can be observed

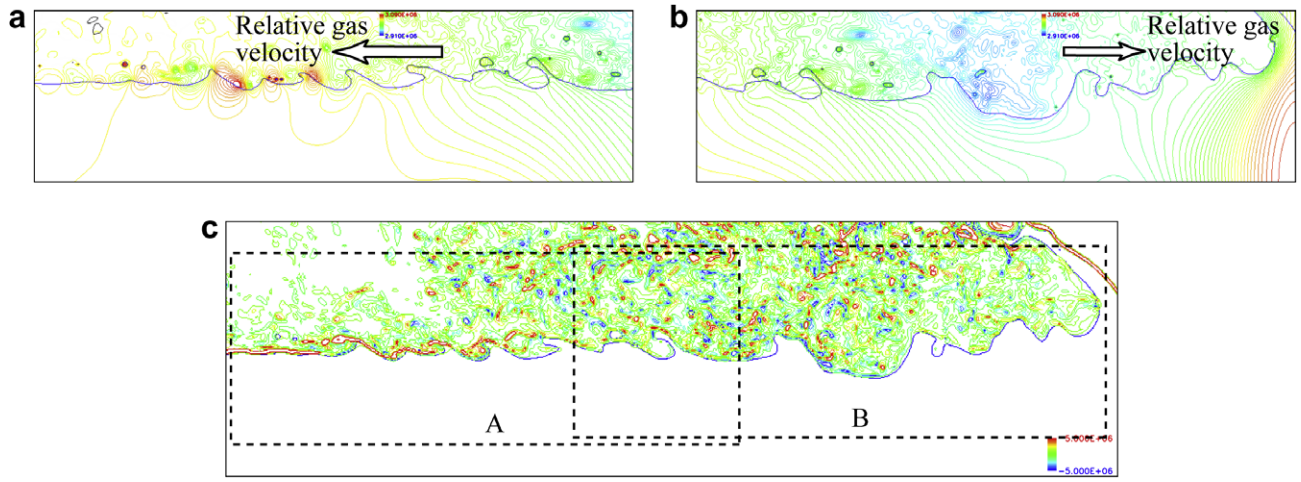

Fig. 18. Pressure and vorticity (z-component) contours. (a) Pressure in region A, (b) pressure in region B, and (c) vorticity. The z-axis is in the normal direction from the paper surface. The white arrows show the local relative gas velocity to the liquid surface.

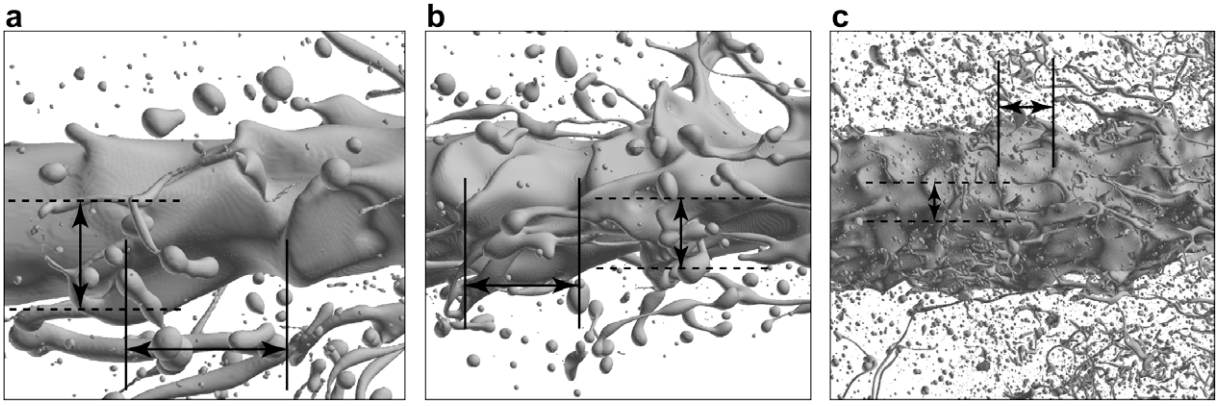

Fig. 19. The surface patterns for each case. (a) Case 1, (b) case 2, and (c) case 3. The solid lines indicate the spatial wavelength of axial mode instability and the dashed lines measure the transverse mode wavelength.

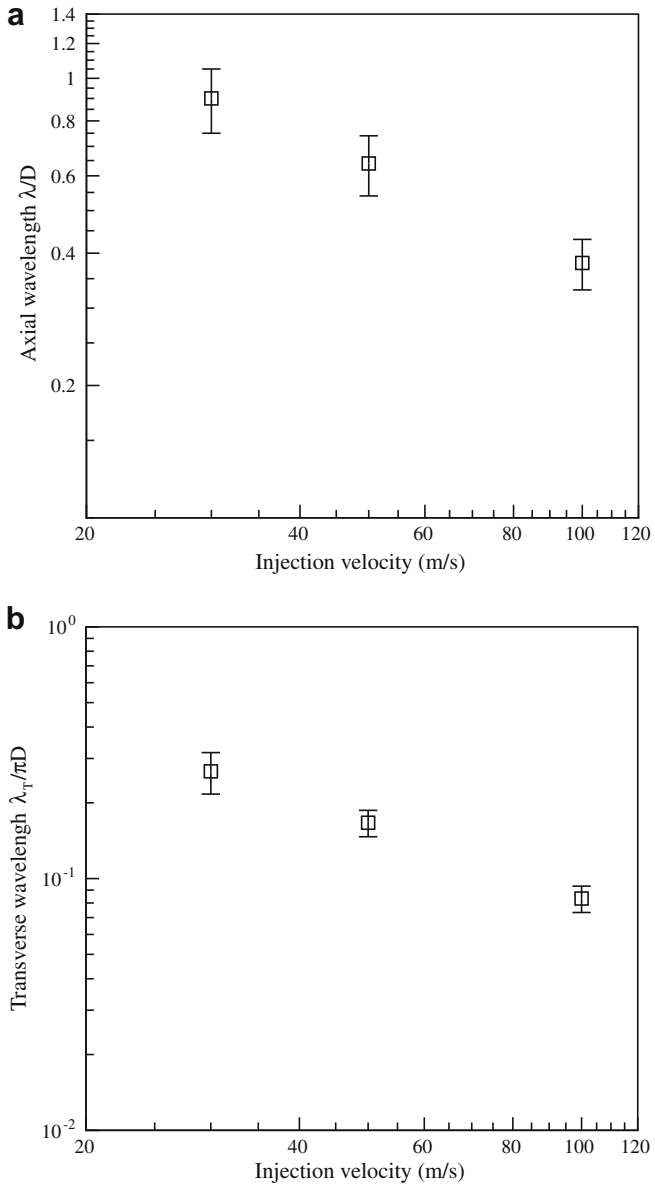

Fig. 20. Length of surface waves in the axial direction and in the transverse direction. (a) Axial direction and (b) transverse direction.

on the surface. At $t = 3.91$, the distinction between the smooth and disturbed regions is discontinuous. As the time passes, the boundary line moves away from the nozzle. This means that ligament and droplet breakup is not determined by the convective growth of nozzle disturbances because the convective distance is not fixed. Breakup can occur only by disturbances from the tip. The boundary is not simply convected due to the disturbed outer gas as shown in Fig. 15e. Fig. 16 shows the temporal plot of the boundary line position. The dashed line indicates mere convection at the injection speed and the boundary motion is slower than the injection speed. The difference means that the size of the region of influence of the tip is spreading toward upstream as the time passes.

Two paths of disturbance transmission toward upstream exist. One path is through the gas phase. As already seen in Fig. 8 or Fig. 15, the region behind the tip is highly disturbed and many vortices are created. By the global recirculation and relative velocity difference, the disturbances are conveyed toward upstream. This can be seen in the axial velocity profiles at several axial positions in Fig. 15e. Another path is through droplet (or ligament) impact. The outer slower velocity region contains many droplets and the re-circulating motion carries some of them toward the liquid surface. The outer droplets are mainly from the tip edge and their axial velocities are lower than the injection velocity. The roll-up vortices behind (upstream of) the jet tip entrain such droplets both toward upstream and toward the core surface, and cause re-collision. Most of the core ligament droplets have the axial velocity comparable to the injection velocity, so they will not propagate upstream. It is also likely that a small portion of the core ligament droplets may be entrained and mixed with the tip edge droplets. As already seen in Fig. 10, droplet re-collision enhances next breakup, thus disturbances are also conveyed upstream. Fig. 17 schematically illustrates the paths. Theoretically, there are waves that propagate on the liquid core surface toward upstream. But the injection speed (*We* number) is very high, so such waves should be very short and viscous damping may overcome very shortly. Thus, propagation through the liquid cannot be dominant.

In the disturbed region, the local relative velocity between the gas phase and the liquid surface is different depending on the location. In the downstream half (region B in Fig. 18), the gas phase velocity is faster. On the other hand, the liquid phase velocity is faster in the upstream half (region A in Fig. 18). The gas shear creates vorticity in the gas phase (Fig. 18c) and wave patterns. In region A, relatively periodic surface waves can be observed. The pressure is high at the downstream crests and low at the troughs.

This is due to the mechanism of the Kelvin–Helmholtz instability. In region B, the flow field is more complicated and the surface patterns are not periodic. Around the trough located at the center of Fig. 18b, lower pressure and negative vorticity can be vaguely seen. In both regions, droplet impact occurs frequently, so disturbances are also generated by impact.

The region A is rather periodic, although the flow field is disturbed. To see the trend of instability, this region is compared between the three cases. Fig. 19 shows the instantaneous liquid core shape for each case. In the axial direction and the transverse direction, wavy patterns can be seen. In both directions, the wavelength becomes smaller as the bulk Weber number increases. Fig. 20 shows the trend.

The present numerical result gives the relative velocity magnitude of $u \sim 0.7U_l$ similarly for the three cases. The observed trend is

$$\lambda \propto u^{-0.71} \tag{12}$$

In the experiment of Marmottant and Villermaux (2004), the trend was

$$\lambda \propto u^{-0.5} \tag{13}$$

The flow conditions are not the same, so direct comparison is difficult. But the trend of negative slope is the same.

For the transverse mode, streamwise vortices are considered to determine the wavelength. The present numerical result gives

$$\lambda_T \propto u^{-0.96} \tag{14}$$

For example by Marmottant and Villermaux (2004), the approximate trend was

$$\lambda_T \propto u^{-1} \tag{15}$$

Thus the basic trend is the same. But quantitative comparison is difficult because the actual flow field is much more complex and further study is needed.

It has been shown that the first-impacted tip area induces the following breakup in the physically straightforward manner. Atomization can naturally occur by this relation of cause (disturbance generation at the tip) and effect (breakup in the upstream region). Of course, if strong disturbances are artificially added to the nozzle flow, atomization may be determined by this external input, i.e., the positions of cause-and-effect can be reversed. But the natural mode is irrelevant to the nozzle.

3.4. Droplet formation from ligament

3.4.1. Droplet formation mechanism

In Section 2.3, we have reviewed the droplet pinch-off dynamics citing our previous research. In this section, the droplet pinch-off dynamics in the sprays is investigated. In actual sprays, as already stated in Introduction, there is no "injection nozzle" for each ligament. Thus, whether the same phenomenon occurs or not should be confirmed. Because the present simulation results have enough grid resolution, this pinch-off process is well captured as shown below.

Fig. 21 shows the droplet formation example in case 1. The white arrows show capillary waves that are already created on this ligament due to surface tension. Which neck is the first to breakup is determined as a result of wave interactions. In this case the neck indicated by the blue arrow in Fig. 21b first breaks up. The red and yellow arrows track the tip pinch-off identified as the short-wave

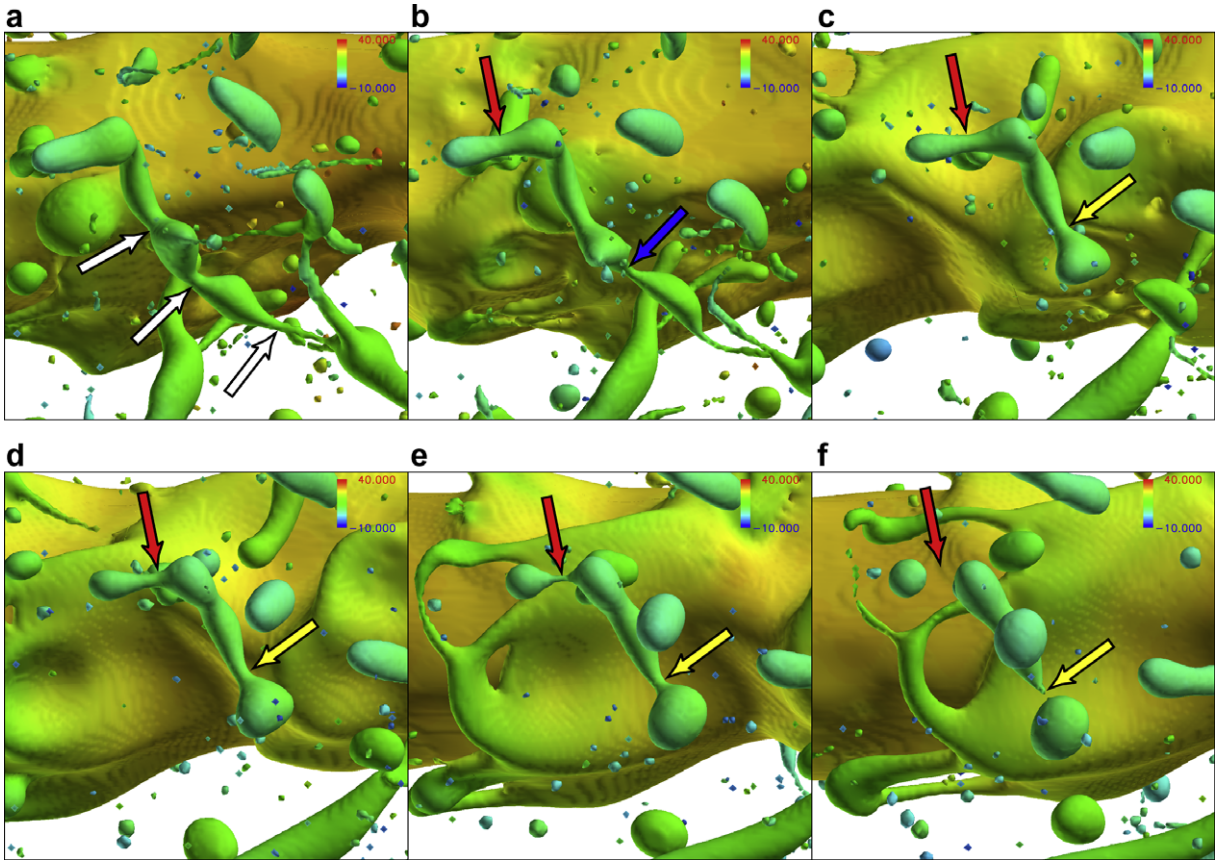

Fig. 21. Droplet formation from ligament (case 1). The color indicates the axial velocity in m/s. The flow is from left to right. (a) $t = 17.57$, (b) $t = 18.27$, (c) $t = 18.97$, (d) $t = 19.67$, (e) $t = 20.37$, and (f) $t = 21.07$.

mode. As a result, the pinch-off wavelength is about 3–4 times the radius of the ligament baseline radius. Note the similarity in the pinch-off dynamics with that shown in Fig. 2.

To see the wave propagation more clearly, the pressure field inside the ligament is shown in Fig. 22 as colored contours on a two-dimensional sliced plane. As in Ref. (Shinjo et al., 2009), the pressure is non-dimensionalized as

$$\Delta p = [p - (p_g + \sigma/a_L)]/(\sigma/a_L) \tag{16}$$

where p_g is the ambient gas pressure and a_L the ligament baseline radius. After $t = 18.27$, a new tip is created at the position of blue arrow. In Fig. 22, the process after this time is tracked.

At $t = 18.97$, due to surface tension, the tip bulb is pushing the ligament toward the central direction. This is the same as stage S-I in Fig. 2c, thus compression waves are emanated from the tip. The tip bulb pressure is high as shown in Fig. 22c by the solid circle. Wavy patterns have already existed before $t = 18.27$ by prior pinch-off motion, so the wave formation (S-I) is faster than starting from a "plain" ligament. The wavelength is about $3.6a_L$, which is exactly the same as that of the steady capillary wave. The tip bulb always becomes larger by the contraction motion, so at $t = 19.67$, the tip bulb pressure is lower than the pressure at $t = 18.27$. (It becomes even lower at $t = 20.37$.) Thus, the ligament is now in stage S-II. The first neck (indicated by the dashed circle) becomes thinner and its pressure becomes higher. This is because the tip bulb sucks the liquid from it as a result of rarefaction wave emanation. Finally, at $t = 20.37$, when the first neck becomes thin enough and its pressure high enough, a local liquid jet from the first neck to the tip bulb emerges and pinch-off occurs.

This motion of pinch-off is exactly the same as the short-wave mode identified in our previous research (Umemura and Wakashima, 2002; Shinjo et al., 2009). The short-wave mode can occur without the injection nozzle. Thus, in a high-speed spray, this mode is also expected to occur naturally for a ligament. In this study, this is confirmed.

A similar and interesting phenomenon can be observed in case 3. For example, the motion of two ligaments is tracked as shown in Fig. 23. The first one is a short and trifurcate one indicated by the red arrow. This ligament is very short, so only the short-wave mode can appear if any pinch-off occurs. As expected, the ligament breaks up into droplets after tip contraction and neck development. This is the same as shown in Figs. 21 and 22.

The other example is indicated by the white arrow. In Fig. 23a, this ligament is about to be separated. In Fig. 23b, the ligament has been formed. In Fig. 23b–d, wave patterns (crests and necks) are developing. It should be noted that these waves develop after the ligament has obtained its tips. The tip bulb is growing at the same time. This means that propagative capillary waves are generated

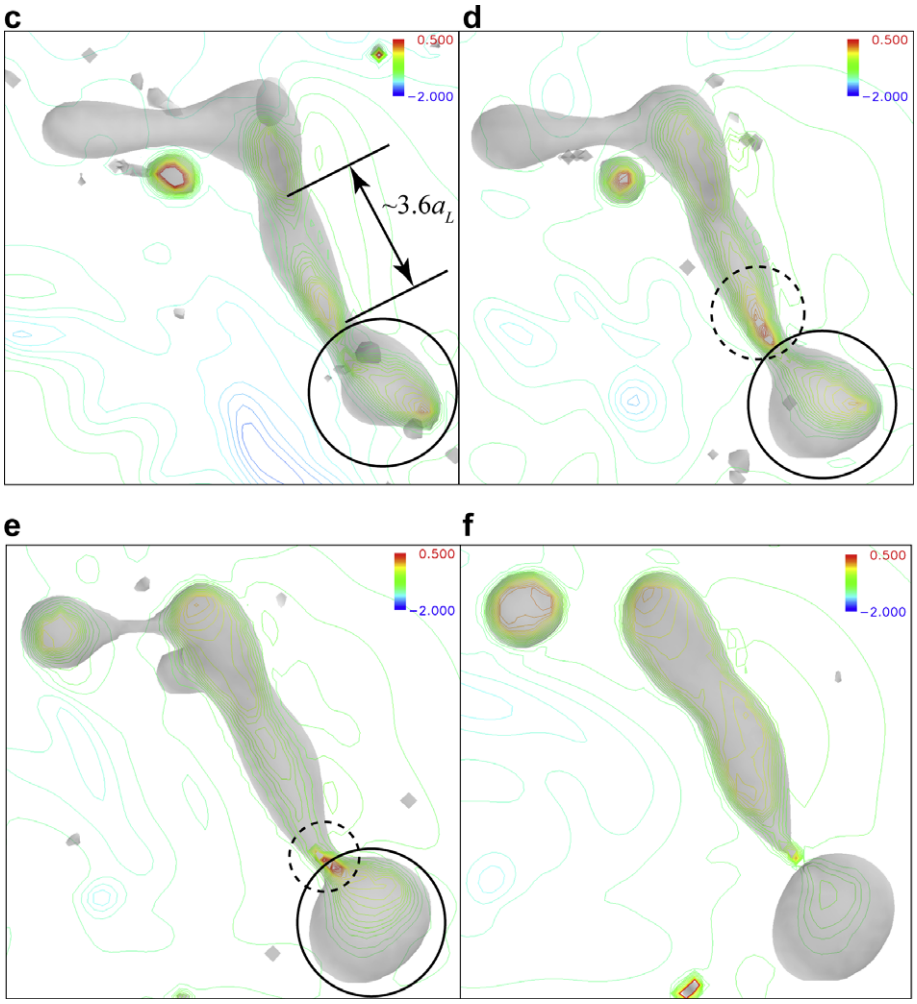

Fig. 22. Droplet formation from ligament (case 1). The ligament in Fig. 21 is picked out and the liquid core in the background is blanked out. The ligament is drawn half-transparently, so other droplets very close to the ligament could not be eliminated. The pressure (Eq. (16)) is drawn on a two-dimensional sliced plane. As the ligament is not perfectly straight, the central axis is not necessarily on the plane. The same naming of (c–f) is used as Fig. 21 ((a) and (b) are not shown here). (c) $t = 18.97$, (d) $t = 19.67$, (e) $t = 20.37$, and (f) $t = 21.07$.

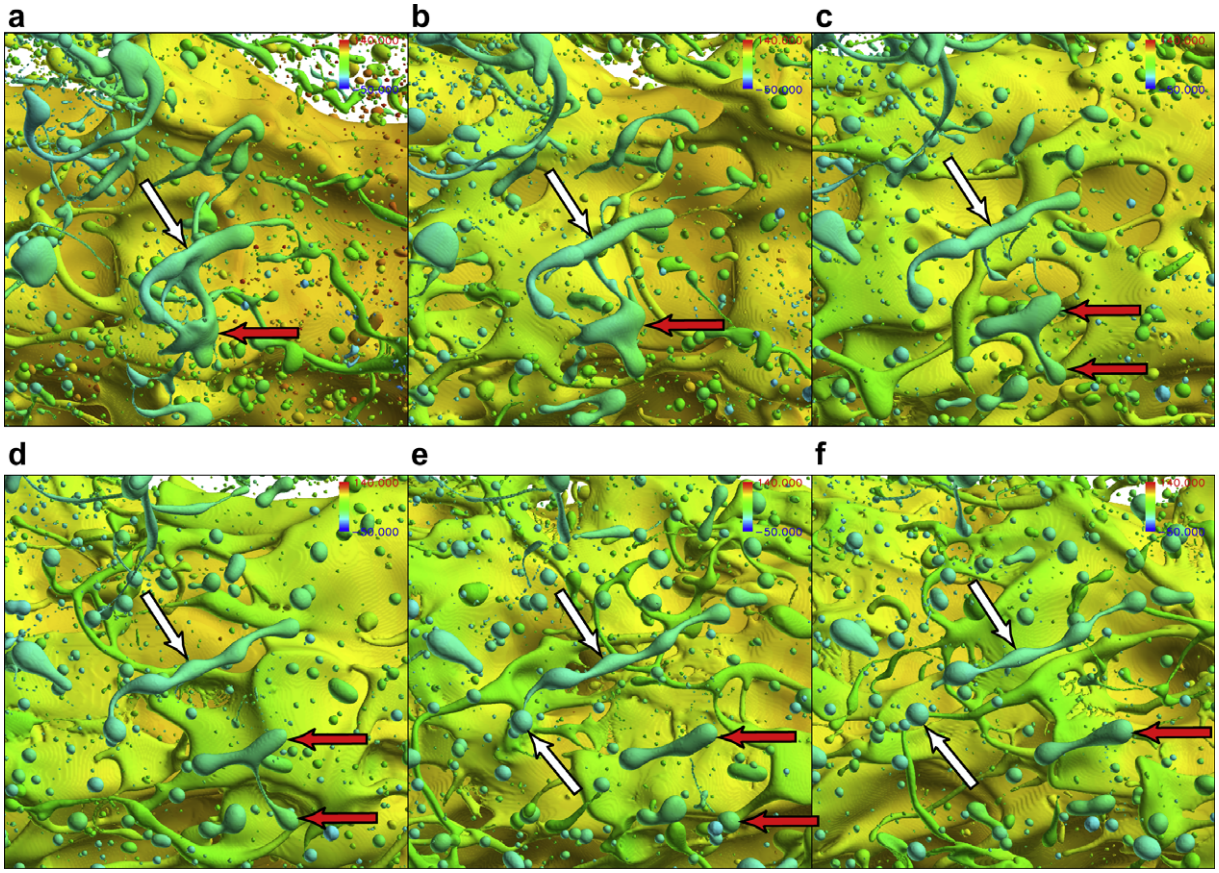

Fig. 23. Droplet formation from ligament (case 3). The color indicates the axial velocity in m/s. The flow is from left to right. The red and white arrows indicate the focused ligaments and generated droplets. (a) $t = 15.25$, (b) $t = 15.90$, (c) $t = 16.55$, (d) $t = 17.20$, (e) $t = 17.84$, (f) $t = 17.99$.

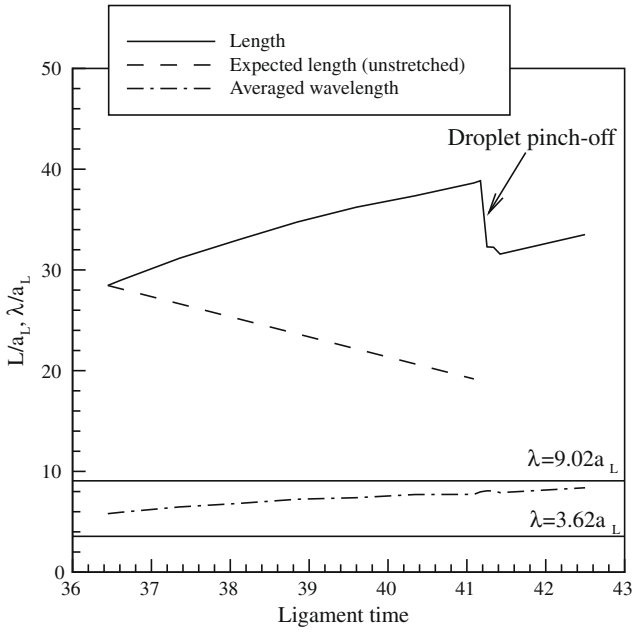

Fig. 24. Temporal trace of ligament length. The solid line indicates the total ligament length and the dash-dotted line the averaged wavelength. Ideal tip contraction (from both ends) gives the dashed line.

by the tip contraction motion. The wavelength measured in Fig. 23c is about 3–4 times the baseline radius of the ligament in some part and a little longer in other part. This is basically the short-wave mode and the elongated wavelength is due to stretch (shown later). The time scale of wave propagation also indicates that this is a short-wave mode. Here, non-dimensional ligament time is scaled as

$$t_L = t_{real}\frac{U_c}{a_L} = t_{real}\frac{1}{a_L}\sqrt{\frac{\sigma}{\rho_l a_L}} \tag{17}$$

where U_c is the propagation velocity of the steady capillary wave (Umemura, 2007a). ($t = 15.25$ is equivalent to $t_L = 35.18$ and $t = 17.99$ to $t_L = 41.49$). The time from ligament formation ($t = 15.83$, not shown in Fig. 23) to wave development ($t = 17.20$) is in the ligament time scale $\Delta t_L = 3.16$, which is close to the ideal propagation period of $\Delta t_L = 3.62$ of the short-wave mode. In Fig. 23e and f, a droplet is finally generated from the tip as indicated by another white arrow.

In Fig. 23e and f, the wavelength on the surface are getting longer than that in Fig. 23c or d. It seems the long-wave mode is present in appearance. However, this is due to ligament stretch. Fig. 24 shows the temporal trace of ligament length l_L. The time is in the ligament time scale t_L. The ligament length (indicated by the solid line) increases as the time passes. The sudden decrease at $t_L = 41.3$ is due to droplet pinch-off. If the ligament is unstretched, the tip should contract at the speed of U_c from both ends. Thus, in $\Delta t_L = 1$, the ligament length will become shorter by $\Delta l_L = 2$. This relation is indicated by the dashed line. The difference means that the ligament is stretched by the local flow field. Because the $We_g \sim O(1)$, tip contraction and stretch occur with similar time scales.

The averaged wavelength gradually increases. Around $t_L = 42.5$ it is about $8.4a_L$. This corresponds to Fig. 25f and the ligament is just before the final stage of pinch-off at all the necks. With this

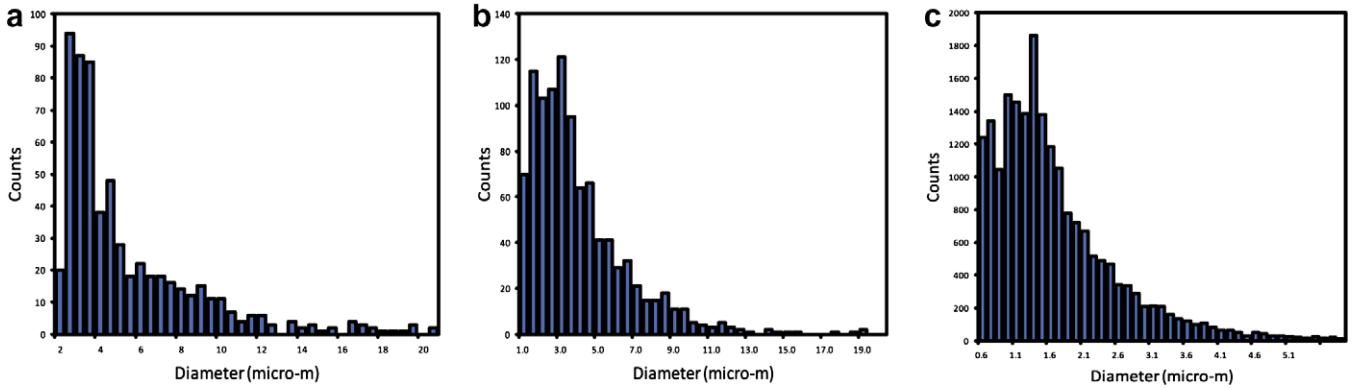

Fig. 25. Droplet size distribution. (a) Case 1 (b) case 2, and (c) case 3. Largely deformed droplets are excluded.

wavelength, the curvature at the neck is smaller in the generating line direction. This leads to relatively stronger surface tension in the circumferential direction, thus pinch-off becomes easier. In fact, this is exactly the very final mechanism of pinch-off in the long-wave or Rayleigh mode. But the above discussion claims that the path to this final state is different, i.e., destabilization is not due to development of the most unstable wave ($\lambda = 9.02a_L$) but due to ligament stretch.

As pointed out by Umemura (2008), conventional laboratory experiments of the Rayleigh instability have utilized the configuration of a slow liquid jet issued in the vertical direction under the normal gravity. The gravitational force naturally stretches the liquid jet, so the results have always included the effect of stretch by the gravity (the effect of injection nozzle is also mixed). Eliminating this effect needs microgravity environment. Recent microgravity experiments by Umemura and Wakashima (2002) excluded the gravity effect and revealed that the Rayleigh instability disappeared in some conditions. This finding finally led to the mechanism in Fig. 3.

Two ligaments have been examined in detail here. Other ligaments also exhibit the same dynamics. The absence of "injection nozzle" (and associated wave reflection) for a ligament makes the selection of the short-wave mode more probable. Whether the Rayleigh instability experiment corresponds to actual ligament situation should be re-considered in this context.

3.4.2. Droplet diameter

As already seen in Fig. 14, the droplet size is expected to become smaller as the bulk *We* increases. The main droplet size is basically larger than the ligament diameter. At the same time, satellite droplets are created, so there are many small droplets. Fig. 25 shows the droplet diameter distribution for each case. The basic distribution profile is similar, while the actual size shifts according to the injection velocity. As pointed out by Herrmann (2009b), droplets of the size of the grid spacing can never be physically obtained as long as the present numerical approach is used. Approximately the five smallest bins of the charts for cases 2 and 3 (seven smallest bins for case 1) may be physically meaningless, considering that the curvature estimation is erroneous for structures made only with 2–3 grid points. The sprays considered here are still in the development phase, thus the values are only for reference.

The Sauter mean diameter (SMD) D_{32} is defined as

$$D_{32} = \sum D_i^3 \Big/ \sum D_i^2 \tag{18}$$

where D_i is the diameter of each droplet. By the simulation data, the SMD for case 1 is 10.8 μm, case 2: 8.0 μm and case 3: 4.3 μm. These values are close to the experimental measurement conducted under similar flow conditions (Wu et al., 1986).

4. Conclusions

The present study has focused mainly on the physical mechanisms from liquid jet injection to droplet formation. By conducting DNS with fine grid resolution, the following findings have been made.

Ligament formation occurs both from the mushroom tip edge and the liquid core surface. The formation phenomenon is very complicated, but shear from local vortices plays an important role. From the mushroom tip edge, quasi-axisymmetric ligaments and streamwise ligaments are generated alternately by the vortex motion. On the liquid core, crests developed by surface instability break into ligaments. Here, shear from vortices also affects the dynamics and multiple ligaments are usually created at one time. The Weber number dependence is clear, i.e., ligaments are created when $We_g \sim O(1)$. Thus, as the bulk *We* number increases, the size of generated ligaments (and droplets) becomes smaller. Re-collision of ligaments and droplets often happens and enhances next breakup.

The initial development of surface instability is caused by the liquid column tip which is first impacted by the gas. Disturbances generated behind the tip mushroom are conveyed toward upstream through the gas phase vortices and also through droplet re-collision. Primary breakup is naturally excited even without external disturbance input.

Droplet formation occurs from the ligament tip mostly by the short-wave mode. Surface capillary wave propagation (or development) is clearly observed and the destabilization process is also the same as observed in the slow liquid jet experiments and simulations. Ligaments are sometimes stretched by the air flow with the same time scale of droplet formation and the apparent wavelength may become longer in such a case. The final shape is close to the long-wave mode shape, but this is the stretched short-wave mode. The dominant mode is the short-wave mode, as is expected from the absence of "injection nozzle" for each ligament. This is confirmed for the first time in this study for high-speed sprays.

In this paper, physical processes occurring in high-speed sprays have been reported, mainly focusing on the dynamics. A next report will deal with statistic characteristics and issues for extension to modeling.

Acknowledgments

One of the authors (J.S.) is grateful to JAXA's Engineering Digital Innovation (JEDI) Center and Fujitsu Supercomputer Operation Team for their support in conducting this large-scale computation.

References

Badock, C., Wirth, R., Fath, A., Leipertz, A., 1999. Investigation of cavitation in real size diesel injection nozzles. Int. J. Heat Fluid Flow, 538–544.

Blaisot, J.B., Yon, J., 2005. Droplet size and morphology characterization for dense sprays by image processing: application to the diesel spray. Exp. Fluids, 977–994.

Brackbill, J.U., Kothe, D.B., Zemach, C., 1992. A continuum method for modeling surface tension. J. Comput. Phys., 335–354.

Chaves, H., Kirmse, C., Obermeier, F., 2004. Velocity measurement of dense diesel fuel sprays in dense air. Atomization Sprays, 589–609.

Desjardins, O., 2009. Detailed numerical investigation of turbulent atomization of liquid jets. ICLASS Paper ICLASS09-053.

Desjardins, O., Moureau, V., Pitsch, H., 2008. An accurate conservative level set/ghost fluid method for simulating turbulent atomization. J. Comput. Phys., 8395–8416.

Fuster, D., Bague, A., Boeck, T., Le Moyne, L., Leboissetier, A., Popinet, S., Ray, P., Scardovelli, R., Zaleski, S., 2009. Simulation of primary atomization with an octree adaptive mesh refinement and VOF method. Int. J. Multiphase Flow, 550–565.

Gorokhovski, M., Herrmann, M., 2008. Modeling primary atomization. Annu. Rev. Fluid Mech., 343–366.

Herrmann, M., 2008a. A balanced force refined level set grid method for two-phase flows on unstructured flow solver grids. J. Comput. Phys., 2674–2706.

Herrmann, M., 2008b. Detailed numerical simulations of the primary breakup of turbulent liquid jets. In: Proceedings of the 21st Annual Conference ILASS-Americas.

Herrmann, M., 2009a. Detailed Numerical Simulations of the Primary Atomization of a Turbulent Liquid Jet in Crossflow. ASME GT2009-59563.

Herrmann, M., 2009b. Detailed Simulations of the Breakup Processes of Turbulent Liquid Jets in Subsonic Crossflows. ICLASS Paper ICLASS09-188.

Herrmann, M., 2009c. The impact of density ratio on the primary atomization of a turbulent liquid jet in crossflow. In: Proceedings of the 62nd APS-DFD.

Himeno, T., Watanabe, T., 2003. Thermo-fluid management under low-gravity conditions (Second report: free-surface flows driven by surface forces). J. Jpn. Soc. Mech. Eng. (Series B), 2400–2407.

Kunugi, T., 1997. Direct numerical algorithm for multiphase flow with free surfaces and interfaces. J. Jpn. Soc. Mech. Eng. (Series B), 1576–1584.

Lebas, R., Menard, T., Beau, P.A., Berlemont, A., Demoulin, F.X., 2009. Numerical simulation of primary break-up and atomization: DNS and modelling study. Int. J. Multiphase Flow, 247–260.

Lin, S.P., 2003. Breakup of Liquid Sheets and Jets. Cambridge University Press.

Linne, M., Paciaroni, M., Hall, T., Parker, T., 2006. Ballistic imaging of the near field in a diesel spray. Exp. Fluids, 836–846.

Marmottant, P., Villermaux, E., 2004. On spray formation. J. Fluid Mech., 73–111.

Menard, T., Tanguy, S., Berlemont, A., 2007. Coupling level set/VOF/ghost fluid methods: validation and application to 3D simulation of the primary break-up of a liquid jet. Int. J. Multiphase Flow, 510–524.

Pai, M.G., Desjardins, O., Pitsch, H., 2008. Detailed Simulations of Primary Breakup of Turbulent Liquid Jets in Crossflow. CTR Annual Research Briefs, Stanford University.

Pan, Y., Suga, K., 2006. Large-eddy simulation of turbulent liquid jets into air. ICLASS Paper ICLASS06-219.

Rantanen, P., Valkonen, A., Cronhjort, A., 1999. Measurements of a diesel spray with a normal size nozzle and a large-scale model. Int. J. Heat Fluid Flow, 545–551.

Sallam, K.A., Dai, Z., Faeth, G.M., 2002. Liquid breakup at the surface of turbulent round liquid jets in still gases. Int. J. Multiphase Flow, 427–449.

Shinjo, J., Umemura A., 2010 (submitted for publication). Detailed simulation of primary atomization mechanisms in diesel jet sprays (Isolated identification of liquid jet tip effects). In: 33rd International Symposium on Combustion.

Shinjo, J., Ogawa, S., Umemura, A., 2007. Characterization of surface wave propagation due to capillary force. J. Jpn. Soc. Aeronaut. Space Sci., 273–281.

Shinjo, J., Matsuyama, S., Mizobuchi, Y., Ogawa, S., Umemura, A., 2009. A numerical study on ligament disintegration mechanism by propagative capillary waves. Atomization, 36–43.

Stahl M., Damaschke, N., Tropea, C., 2006. Experimental investigation of turbulence and cavitation inside a pressure atomizer and optical characterization of the generated spray. ICLASS Paper ICLASS06-116.

Stone, H.A., 1994. Dynamics of drop deformation and breakup in viscous fluids. Annu. Rev. Fluid Mech., 65–102.

Stone, H.A., Leal, L.G., 1989a. Relaxation and breakup of an initially extended drop in an otherwise quiescent fluid. J Fluid Mech., 399–427.

Stone, H.A., Leal, L.G., 1989b. The influence of initial deformation on drop breakup in subcritical time-dependent flows at low Reynolds numbers. J. Fluid Mech., 223–263.

Stone, H.A., Bentley, B.J., Leal, L.G., 1986. An experimental study of transient effects in the breakup of viscous drops. J Fluid Mech., 131–158.

Suh, H.-K., Lee, C.-S., 2008. Effect of cavitation in nozzle orifice on the diesel fuel atomization characteristics. Int. J. Heat Fluid Flow, 1001–1009.

Sussman, M., Puckett, E.G., 2000. A coupled level set and volume-of-fluid method for computing 3D and axisymmetric incompressible two-phase flows. J. Comput. Phys., 301–337.

Sussman, M., Smereka, P., Osher, S., 1994. A level set approach for computing solutions to incompressible two-phase flow. J. Comput. Phys., 146–159.

Takewaki, H., Nishiguchi, A., Yabe, T., 1985. Cubic interpolated pseudo-particle method (CIP) for solving hyperbolic-type equations. J. Comput. Phys., 261–268.

Umemura, A., 2004a. Microgravity research on liquid jet instability. J. Jpn. Soc. Microgravity Appl., 293–299.

Umemura, A., 2004b. Micro-gravity study on instability of near-critical mixing surface jet (mechanisms of Rayleigh–Taylor instability excitation at nozzle exit and short spacing disintegration). J. Combust. Soc. Jpn., 50–59.

Umemura, A., 2007a. Self-destabilizing mechanism of circular liquid jet (first report: capillary waves associated with liquid jet destabilization). J. Jpn. Soc. Aeronaut. Space Sci., 216–223.

Umemura, A., 2007b. Self-destabilizing mechanism of circular liquid jet (second report: proposal of breakup feedback loop model). J. Jpn. Soc. Aeronaut. Space Sci., 224–231.

Umemura, A., 2007c. Self-destabilizing mechanism of circular liquid jet (third report: model simulation of liquid jet disintegration process). J. Jpn. Soc. Aeronaut Space Sci., 359–366.

Umemura, A., 2008. Impacts on liquid atomization theory from microgravity experiment. J. Jpn. Soc. Microgravity Appl., 50–57.

Umemura, A., Wakashima, Y., 2002. Atomization regimes of a round liquid jet with near-critical mixing surface at high pressure. Proc. Combust. Inst., 633–640.

Wu, K.-J., Reitz, R.D., Bracco, F.V., 1986. Measurements of drop size at the spray edge near the nozzle in atomizing liquid jets. Phys. Fluids, 941–951.